Paris-Saclay University

Reducing suspension thermal noise in Gravitational Waves interferometers using a Sample Convolution and Interaction Network (SCINet)

Internship report

Pierre CAVALIER

Supervised by:

TAKAHASHI Hirotaka, MEYER-CONDE Marco

September 28, 2024

Acknowledgements

I would like to express my gratitude to all the people who have supported and accompanied me throughout my internship at the Tokyo City University. I would also like to thank the people at Paris-Saclay University who made this internship abroad possible, notably by agreeing to shorten its duration, thank you Mrs Keribin.

First of all, I'd like to thank my internship tutor, Hirotaka Takahashi-sensei, for giving me this incredible opportunity to work on the KAGRA project in Japan. Thank you for guiding me in my work, making it all the more interesting.

I'd also like to thank Marco Meyer-Conde for making himself available on a very regular basis, and for helping me with the many problems I was able to overcome. His comments were always pertinent and enabled me to move forward, to progress both in my work and personally.

I want to express my sincere gratitude to Kentaro Komori-san for the insightful discussions on the KAGRA suspension system. His collaboration has significantly helped me progress in my research.

My thanks go to all the members of the Gravitational Wave Physics and Astronomy/Data Science Group, with whom I've been able to exchange ideas on a regular basis and discuss subjects that go beyond the internship, and I'd like to thank you for your contribution.

This internship has been a formative and incredible experience, and I'm know for a fact that it will have a significant impact on my future professional development. Thank you to everyone who helped make this experience possible.

Contents

1 Introduction

Gravitational waves are ripples in space-time, generated by cataclysmic cosmic events such as the collision of black holes or the merging of neutron stars. They propagate through the universe at the speed of light. Gravitational waves make it possible to observe events in space by means other than electromagnetic waves.

Gravitational waves are a consequence of Einstein's 1915 theory of general relativity. According to this theory, massive objects distort space-time, and when these objects move at accelerated speeds, they create disturbances that propagate as waves. Einstein himself believed that these waves would be too weak to ever be detected [4].

The Laser Interferometer Gravitational-Wave Observatory (LIGO) is the first gravitational-wave observatory to be built: one in Hanford, denoted H1, Washington, USA, and one in Livingston, denoted L1, Louisiana. They were inaugurated in 2002, after more than 30 years of planning. We will have to wait until September 14, 2015 at 9 h 50 min 45 s UTC to observe the first black hole merger, namely, GW150914, at 450 MegaParsec (1 MegaParsec = 1Mpc = 3.262×10^6 light-years), i.e. over a billion light-years away, which will have been made on both detectors. The European Virgo detector, located in Cascina, Italy, and inaugurated in 2003, was unable to detect GW150914.

This discovery earned Rainer Weiss, Kip Thorne and Barry Barish a Nobel Prize in 2017 for their key role in the design, construction and operation of the LIGO project. Takaaki Kajita, the 2015 Nobel laureate in Physics for his work on neutrinos, is the principal investigator of the Kamioka Gravitational Wave Detector (KAGRA), a gravitational wave observatory established in Japan. Initially approved as the LCGT project in 2010, it was renamed KAGRA in 2012. The observatory itself was established in 2016, and the KAGRA experiment was finalized in 2019. It aims to introduce new cryogenic cooling technology compared to other observatories and made its first observation in 2020.

As the amplitudes of gravitational waves are very low compared to ambient noise, it is necessary to reduce the latter as much as possible. One method aiming to reduce seismic noise is to suspend the detector components on complex machinery, which helps isolate them from ground vibrations. However, this approach comes with a trade-off: while it improves isolation, it also introduces additional mechanical resonances that can affect the sensitivity of the detector at specific frequencies. This introduces a new type of noise, the suspension noise.

The latter is characterized by peaks of high intensity at a given resonance frequency, with a finite width determined by the damping characteristics, typical of a damped oscillator. To solve this problem, one of the solutions being explored is machine learning signal processing, with the aim of eliminating the peak in real time, without altering the information contained in the signal.

2 Gravitational Waves Physics

2.1 Gravitational theories

Gravity is one of the four elementary interactions, alongside the strong nuclear interaction, the electromagnetic interaction and the weak interaction. In 1687, Newton's law of universal gravitation was published, expressing the gravitational force in the following manner:

$$\vec{F} = -G\frac{m_1 m_2}{\|\vec{r}\|^3}\vec{r} \tag{2.1}$$

Where:

- $\vec{F}$ is the vector gravitational force
- G is the gravitational constant
- m_1 and m_2 are the masses of the two objects
- $\vec{r}$ is the vector between the two objects

Newton's law of gravitation, although extremely accurate for objects of moderate size and low velocities ($v \ll c$), has its limits under extreme conditions. It doesn't take relativistic effects into account, making it inapplicable to very massive objects, such as black holes, or in situations where velocities approach that of light. During Einstein's annus mirabilis, the article on general relativity proposed a revolutionary description of gravitation. Unlike Newton's gravitation, it is based on the idea that gravitation is not a force but the result of the curvature of space-time, a four-dimensional structure encompassing space and time. This curvature is produced by the presence of matter and energy. Key ideas in general relativity include:

- Equivalence Principle: It states that locally (in small enough regions of spacetime), the effects of gravity are indistinguishable from those of acceleration. An object in free fall does not feel gravity, just like someone in a spaceship accelerating in space would feel like they are under the influence of gravity.
- Spacetime Curvature: Matter and energy determine the curvature of spacetime, which is described by the metric tensor $g_{\mu\nu}$. The curvature of spacetime affects how matter and light move through it.

Einstein's field equations describe this relationship between matter/energy and the curvature of spacetime. They are given by the following equation:

$$G_{\mu\nu} + \Lambda g_{\mu\nu} = \frac{8\pi G}{c^4} T_{\mu\nu} \tag{2.2}$$

- $G_{\mu\nu}$ is called the Einstein tensor, which represents the curvature of spacetime.
- Λ : is the cosmological constant. It represents a cosmic repulsion force acting on large scales. It is neglected in our context as it relates on dark matters/energy.
- $g_{\mu\nu}$: The metric tensor, which describes the geometric structure of spacetime. It tells how distances are measured and how spacetime is curved.
- c is the speed of light in vacuum
- $T_{\mu\nu}$: The stress-energy tensor (also known as energy-momentum tensor), which describes the distribution of matter, energy, momentum, and stress in spacetime. It serves to describe the dynamics of spacetime curvature. In presence of heavy objects (Black Hole, Neutron Star), the tensor becomes significant.

According to Einstein's theory of general relativity, the line element of curved space time geometry, denoted ds, can be described as infinitesimal displacement vector and defined as:

$$ds^2 = g_{\mu\nu}\, dx^\mu\, dx^\nu \tag{2.3}$$

The metric tensor of curved spacetime can be expressed like this:

$$g_{\mu\nu} = \eta_{\mu\nu} + h_{\mu\nu} \tag{2.4}$$

With $\eta_{\mu\nu}$ corresponding to the Minkowski metric and dx the space metric. In Minkowski space, in 4-dimensional spacetime, it is often written as:

$$\eta_{\mu\nu} = \begin{pmatrix} -1 & 0 & 0 & 0 \\ 0 & 1 & 0 & 0 \\ 0 & 0 & 1 & 0 \\ 0 & 0 & 0 & 1 \end{pmatrix}, \quad dx^\mu = dx^\nu = \begin{pmatrix} dt \\ dx \\ dy \\ dz \end{pmatrix} \tag{2.5}$$

Here, we consider $h_{\mu\nu}$ as a deformation of the spacetime.

For simplification purposes, Einstein introduces an algebraic short-hand notation also known as Einstein Notation. It states that when an index is repeated in both covariant (lower) and contravariant (upper) position in a product of two terms, it implies a summation over the N index (in spacetime $N = 3$ with 0 representing time and 1, 2 and 3 spatial coordinates).

$$A^\mu B_\mu = \sum_{\mu=0}^{N} A^\mu B_\mu \tag{2.6}$$

Here are typical notations and tensor operations:

- Index position switch (using metric tensor for instance) $V_\mu = g_{\mu\nu} V^\nu$
- In standard notation, the contraction of $T^{\mu\nu}$ with $g_{\mu\nu}$ can be written out explicitly: $\sum_{\mu=0}^{3} \sum_{\nu=0}^{3} T^{\mu\nu} g_{\mu\nu}$. In Einstein notation, it becomes $T^{\mu\nu} g_{\mu\nu}$.
- In the specific case for trace contraction: $T^\mu_\mu = \sum_{\mu=0}^{3} T^\mu_\mu$

For an observation from Earth, we consider ourselves far from source and in a vacuum region. That leads to the second term and the third term of the equation close to zero and therefore the Einstein Field Equation (2.2) becomes simply:

$$G_{\mu\nu} = 0 \tag{2.7}$$

The Einstein tensor can be written as follows: $G_{\mu\nu} = R_{\mu\nu} - \frac{1}{2} R g_{\mu\nu}$ with $R_{\mu\nu}$ the Ricci Tensor, that measures the way in which the curvature of space-time.

The wave equation for the perturbation approximation of the metric tensor is given by :

$$\Box h_{\mu\nu} = 0 \qquad \text{where} \quad \Box = \frac{\partial^2}{\partial t^2} - \nabla^2 \tag{2.8}$$

The solutions of this equation in vacuum are plane waves of the form:

$$h_{\mu\nu}(t, \vec{x}) = A_{\mu\nu} e^{i(k_\sigma x^\sigma)} \tag{2.9}$$

2.2 Definition of Gravitational Waves

Let us consider a Gravitational wave traveling in the z-direction,

$$k_\sigma = (-\omega, 0, 0, k).$$

Where:

- ω is the angular frequency or pulsation of the wave.
- k is called the wave vector, it's the wave's spatial angular frequency.

As in the case of electromagnetism, the wave propagation solution can be decomposed into two independent components representing two polarization modes, h_+ and $h_\times$:

$$h_{\mu\nu}(t,\vec{x}) = \begin{pmatrix} 0 & 0 & 0 & 0 \\ 0 & h_+ & h_\times & 0 \\ 0 & h_\times & -h_+ & 0 \\ 0 & 0 & 0 & 0 \end{pmatrix} \exp i(-\omega t + kz) \tag{2.10}$$

This leads to two polarizations, corresponding to two modes of spatial deformation of space-time, often referred to as plus mode + and cross modes ×. These deformations describe the oscillation of the $g_{\mu\nu}$ tensor, which causes successive squeezing and stretching of spacetime. In the orthonormal reference frame of space-time $(\hat{e}_0, \hat{e}_1, \hat{e}_2, \hat{e}_3)$, we can describe the perturbation vectors of the two different modes.

$$e^+_{ij} = \hat{e}_1 \otimes \hat{e}_1 - \hat{e}_2 \otimes \hat{e}_2, \tag{2.11}$$

$$e^\times_{ij} = \hat{e}_1 \otimes \hat{e}_2 + \hat{e}_2 \otimes \hat{e}_1. \tag{2.12}$$

In the following reference frame defined by equations (2.11) and (2.12), deformations of a gravitational z-direction was perpendicular to the sheet/screen can be seen in figure 2.1. The pattern from h_+ to $wt = \frac{\pi}{2}$, when the oscillatory argument of the wave reaches 90 degrees, corresponds to a maximum squeezing along the y axis and a stretching along the x axis, and similarly, at $wt = \frac{3\pi}{2}$ corresponds to stretching along the y axis and a squeezing along the x axis.

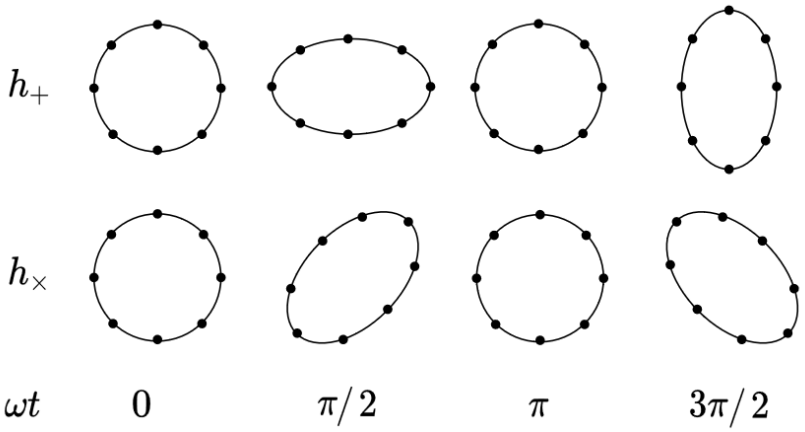

Figure 2.1: Illustration of the effect of the plus and cross propagation of GWs [12]

Gravitational waves can be classified into 4 types, model and unmodeled as well as transient and continuous:

- Continuous Gravitational Waves: These waves originate from continuous sources, such as asymmetric neutron stars spinning on themselves. Unlike inspiral waves, they have regular frequencies and don't vary much over time.
- Stochastic Gravitational Waves: They are the relic gravitational waves from the early evolution of the universe. Much like the Cosmic Micro-wave Background, which is likely to be the leftover light from the Big Bang.
- Burst Gravitational Waves: These waves result from sudden, violent events such as supernovas, mergers of compact objects or mountain ruptures on neutron stars. They are transient, producing a brief but intense signal.
- Compact Binary Coalescences Gravitational Waves: These waves are emitted by Compact Binary Coalescences (CBC). CBC refer to the merging events of two compact astronomical objects, such as black holes, neutron stars,

or a black hole and a neutron star. These objects are referred to as compact due to their dense nature. In those merging events, there are three different successive phases : inspiral, merger and ringdown.

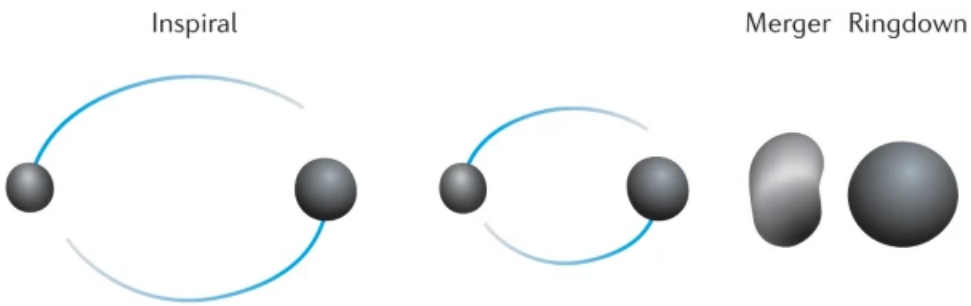

Figure 2.2: Visualisation of a Binary Merger

The gravitational waves that interest us and that we know how to model are those that correspond to massive binary systems, e.g. black hole and neutron star mergers. There are three phases, as shown in the figure 2.2:

- Inspiral phase: when the two black holes orbit each other and come closer together due to the gravitational waves they emit.
- The merger phase: when the two black holes merge into a single black hole. This phase corresponds to an amplitude peak.
- The ringdown phase: when the resulting black hole stabilizes, emitting a few more oscillations before reaching a stable final state.

3 Gravitational Waves Observatory: LIGO-VIRGO-KAGRA

LIGO, Virgo and KAGRA (LVK) form the advanced network of gravitational wave detectors. LIGO is managed by the LIGO Laboratory, a consortium of the California Institute of Technology (Caltech) and the Massachusetts Institute of Technology (MIT)? Virgo is operated by the European Gravitational-Wave Observatory and KAGRA by The Institute for Cosmic Ray Research (ICRR), the High Energy Accelerator Research Organization (KEK) and National Astronomical Observatory of Japan (NAOJ). On the map (Fig. 3.1), there is also the detector GEO600 in Hannover in Germany, which is a stepping stone in research. The technologies are being developed and tested as part of the GEO project for implementation in other GW observatories. They are also used simultaneously with these observatories. They also make simultaneous runs with those observatories. Together, they detect, locate and characterize the coalescence of compact binary mergers, continuous gravitational waves and burst gravitational waves. This manuscript will be focusing mainly in the perspective of KAGRA interferometer.

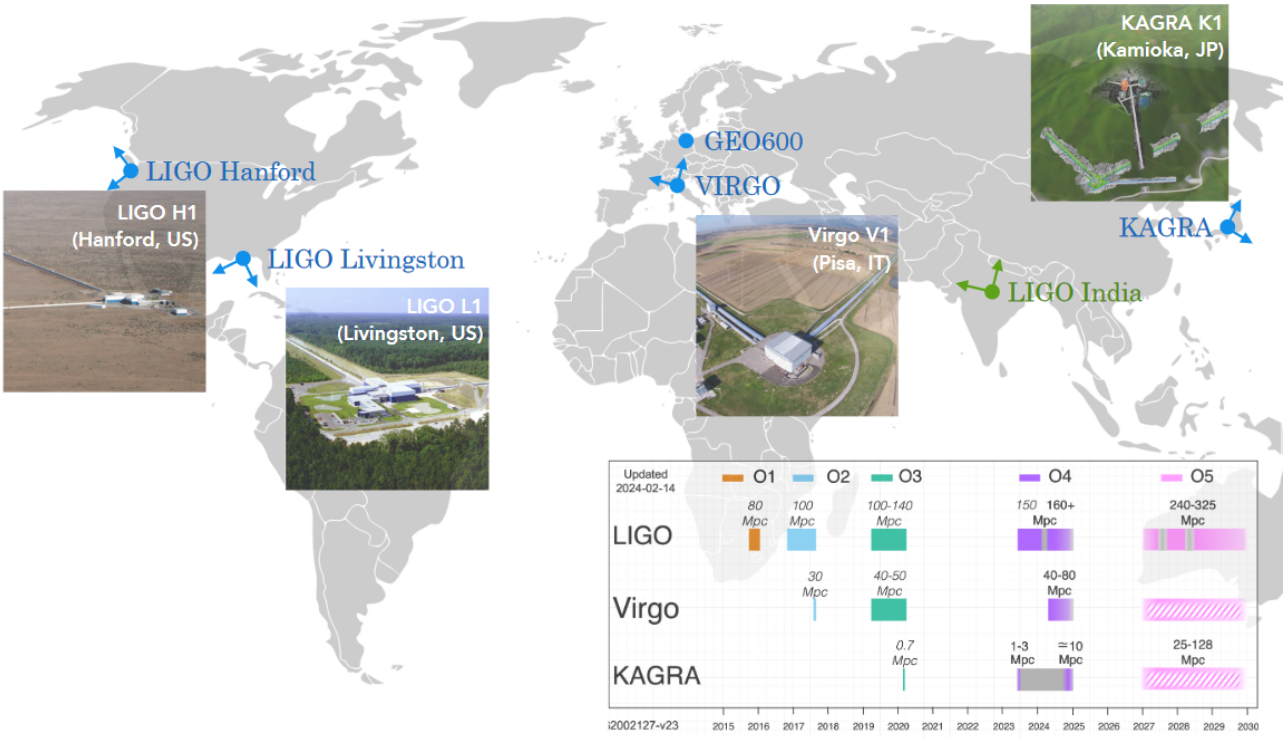

Figure 3.1: Detector localizations (world map) and the observing plan (bottom-right)

The LVK collaboration brings together ground-based gravitational wave telescopes. Their location and placement allow detectors to complement each other and cover a wider area of the skymap. A larger number of detectors increases the quality of the sky map, and better sensitivity by reducing noise, ultimately enabling an event to be measured with a standard telescope using the NASA General Coordinates Network reporting system. In addition, other projects are being planed such as the Laser Interferometer Space Antenna (LISA), which is a detector in space that would allow a better sensitivity and a better frequency range, or the Einstein Telescope, the next generation gravitational wave detector.

At the bottom left of the figure 3.1 is the observing plan, which represents the different observing runs of the detectors. Oi corresponds to the i-th observation run, of which the 4th is still in progress with O4b until early 2025. In this timeline, distances given in Mpc (1 Megaparsec = 3.262×10^6 light-years) refer to the binary neutron star range, indicating the detection capabilities for such events. Binary black hole (BBH) mergers, being louder, can typically be detected at much greater distances.

3.1 Michelson Interferometer Principle

Laser interference is a key phenomenon in wave physics, resulting from the superposition of two or more waves. When coherent photons meet, they can interact constructively or destructively, depending on their relative phase, creating patterns of reinforcement or cancellation.

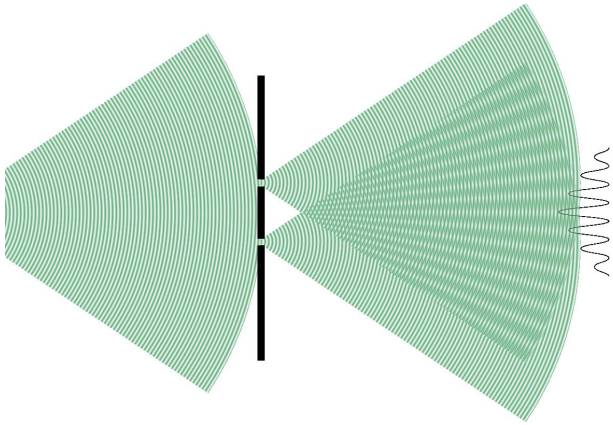

Figure 3.2: Young's Experience

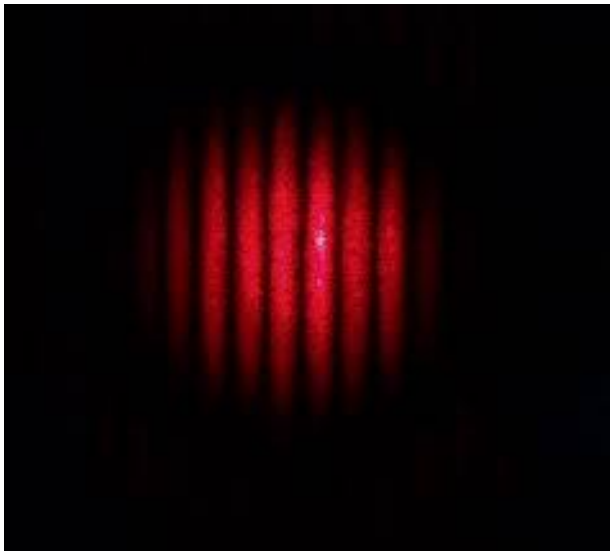

Figure 3.3: Interference pattern

The Young's slit experiment, a coherent light source, usually a lamp or laser beam, is directed onto an opaque barrier with two thin parallel slits. The light passing through these slits (Fig 3.2) is then projected onto a screen (Fig 3.3) placed behind the barrier.

The two waves emanating from the slits are superimposed and interfere with each other. When the crests of the wave from one slit coincide with the crests of the wave from the other slit, constructive interference occurs, forming bright areas on the screen. Conversely, when the peaks of one wave coincide with the troughs of the other, destructive interference occurs, resulting in dark areas.

Without going into the details of the calculations, we can describe the characteristics of the interference pattern. Depending on where you place an intensity detector, you can measure the phase shift between the two signals, which is where the idea for the Michelson interferometer came from:

A Michelson interferometer consists of at least two mirrors, $M1$ and $M2$, and a beam splitter, usually a 50% reflective mirror M. A coherent light source, like a laser, S emits a beam which reaches the beam splitter. Since M is partially reflective, some of the light is transmitted to point B, while some is reflected back to point A. The two beams reflect off the $M1$ and $M2$ mirrors respectively, then recombine to produce an interference pattern on the E detector.

Since gravitational waves are a perturbation of space-time, the passage of one of them through the detectors will introduce a change in the length between the two arms of the detector. Therefore, a gravitationnal wave going inside the detector will modify the interference pattern enabling ΔL to be calculated. It's important to note that the length of the arms L, will also influence the sensitivity of the device, the longer the arms, the better the sensibility will be.

3.2 KAGRA Experiment

The KAGRA collaboration is an international initiative involving some 400 scientists and engineers from over 100 institutions in 15 countries. It was founded in 2010 under the leadership of the Institute for Cosmic Ray Research at

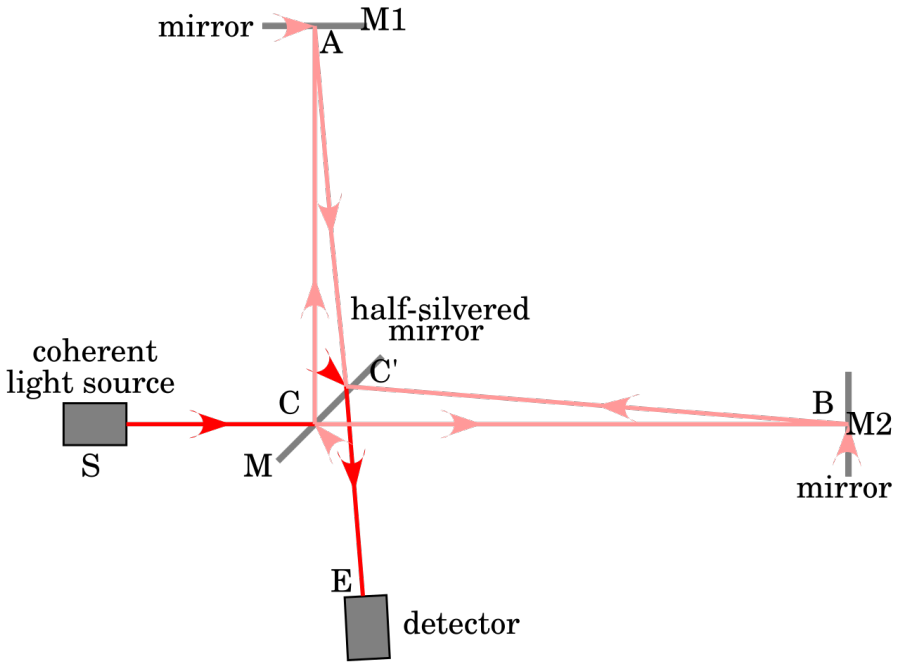

Figure 3.4: Michelson interferometer

the University of Tokyo. KAGRA is the first underground gravitational wave detector, located in Kamioka, Japan, and uses cryogenic technology to cool its mirrors to 20 Kelvins, reducing interference from thermal noise. Its arms are 3 kilometers, which is the same as VIRGO and less than LIGO (4 kilometers) in order to improve the sensitivity of the detector.

Figure 3.5: Kagra Location

The reason why KAGRA is located underground in the mountains is to reduce environmental noise, such as seismic noise, and improve the accuracy of its measurements. The configuration of KAGRA is described in the article *Performance of the KAGRA detector during the first joint observation with GEO 600 (O3GK)* [2].

3.2.1 Hardware

The KAGRA interferometer works on the same principle as a Michelson interferometer, with additional modifications to better performances, and considering the large device size as compared to the human size Michelson toy model introduced in section 3.1 (view Fig 3.6). PRM, PR2, et PR3, SR2 and SR3 components correspond to the power-recycling cavity length that improve detection and sensitivity. The OMC cleans the spatial mode and rejects unwanted signal.

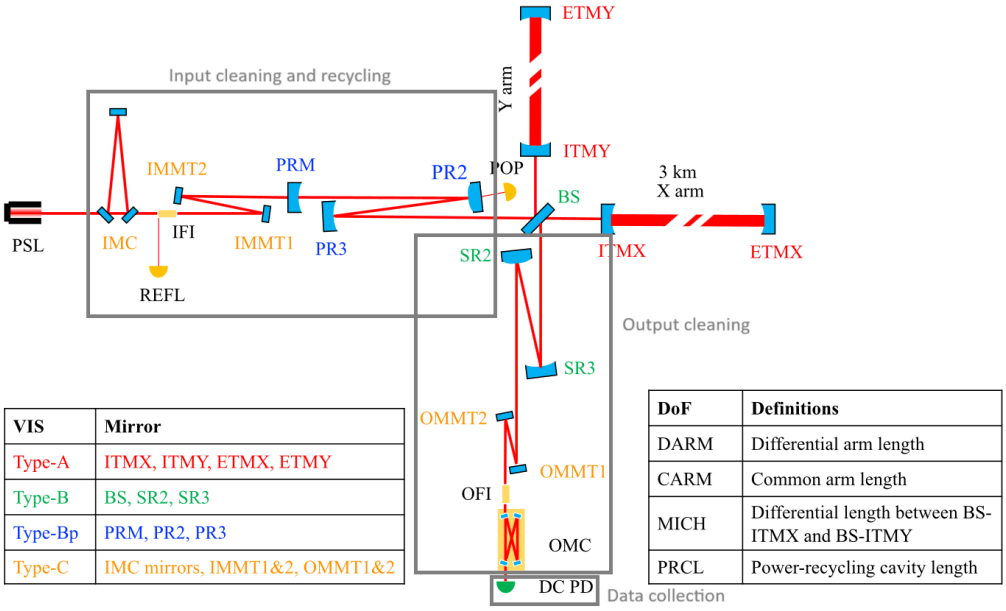

VIS	Mirror
Type-A	ITMX, ITMY, ETMX, ETMY
Type-B	BS, SR2, SR3
Type-Bp	PRM, PR2, PR3
Type-C	IMC mirrors, IMMT1&2, OMMT1&2

DoF	Definitions
DARM	Differential arm length
CARM	Common arm length
MICH	Differential length between BS-ITMX and BS-ITMY
PRCL	Power-recycling cavity length

Figure 3.6: Kagra Interferometer

3.2.2 Focus: Seismic Isolation System

In addition to KAGRA's underground location, complex engineering is in place to reduce systemic vibration. It uses a multi-stage suspension system, in particular for the sapphire mirror ITM[XY] and ETM[XY] (Type-A suspension), to suspend the mirrors. Each mirror is suspended by a series of cables and secondary masses that act as dampers to isolate the mirror from earth vibrations. This multi-stage design helps to reduce vibrations at each level.

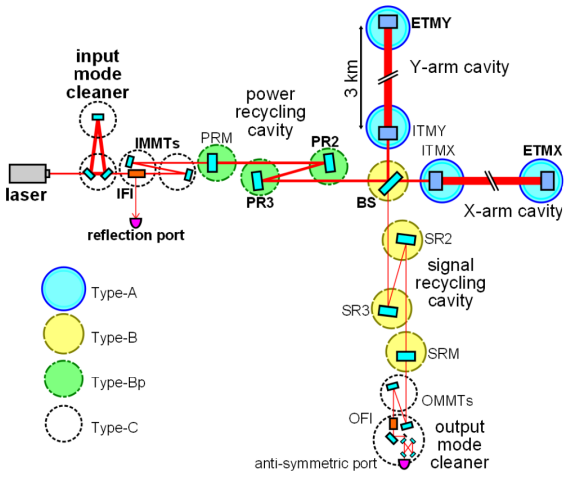

Figure 3.7: Suspension in KAGRA's Michelson Interferometer

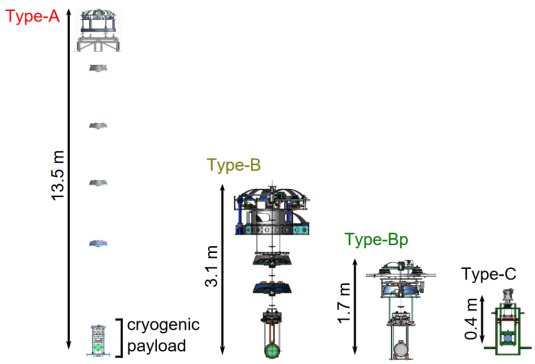

Figure 3.8: Suspensions used at KAGRA

As shown in figure 3.7, there are several types of suspension and the ones we are interested in are the longest, and therefore the most likely to generate noise, i.e. type A suspension (referring to figure 3.8).

3.2.3 Strain measurement

The key quantity measured is the **strain**, represented as $\frac{\Delta L(t)}{L}$, which describes the relative displacement between the two detector arms. Gravitational wave strain $h(t)$ comes from differential arm motion (DARM) with $\Delta L(t) = \frac{1}{2} L \times h(t)$ where L the arm length. By comparing the initial signal emitted by S with that received by E, we can determine the quantity $\Delta L = \frac{L_x - L_y}{2}$, which captures the change in length between the two arms. The strain signal $h(t)$ of a GW signal is given, taking into account the antenna pattern functions F_+ and $F_\times$ as:

$$h(t) = F_+(\theta, \phi, \psi, t) h_+(t) + F_\times(\theta, \phi, \psi, t) h_\times(t), \tag{3.1}$$

where θ is the right ascension, ϕ is the declination, and ψ is the polarization angle, represented in figure 3.9. These strain measurements are taken successively, with each separated by a time interval $\Delta t = \frac{1}{f_s}$, where f_s is the detector's sampling frequency.

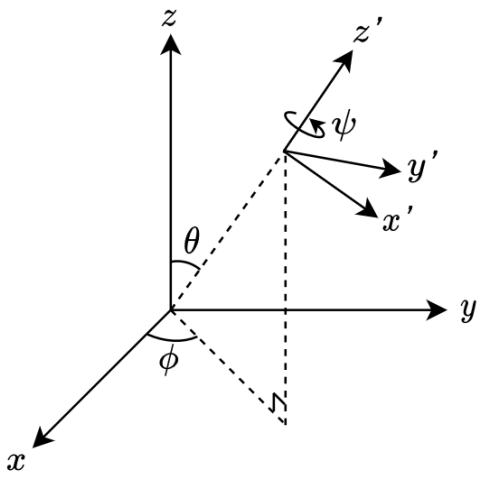

Figure 3.9: Relative orientation of the source and sky frames. θ, ϕ and ψ express the transition from one referential to another

The phase difference is induced time of flight between interferometers and the interferometer orientation.

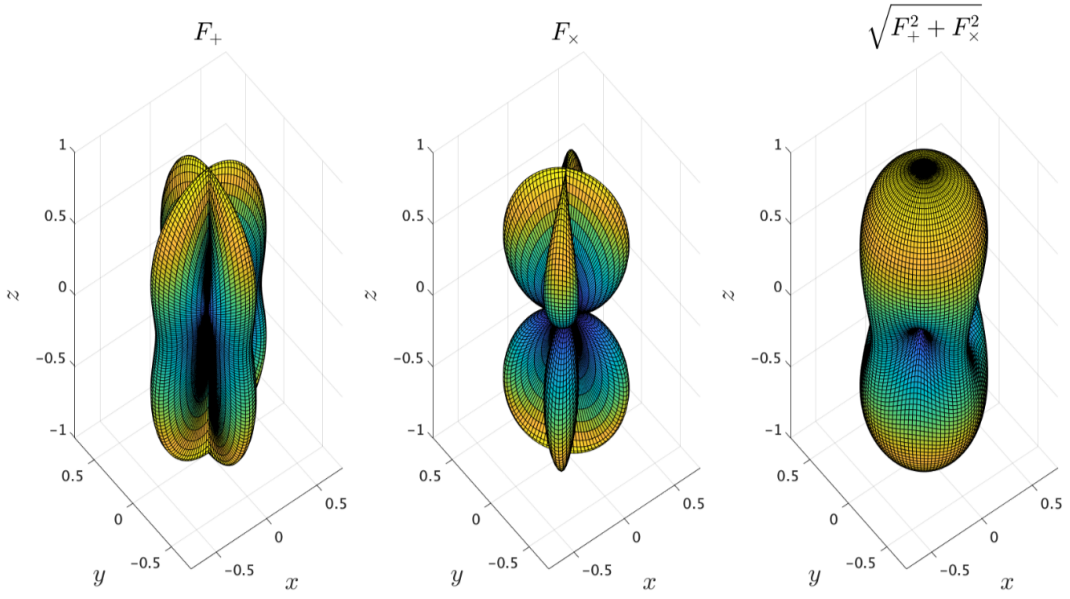

Figure 3.10: Antenna pattern of KAGRA

To describe the Michelson interferometer's sensitivity to the plus and cross polarizations of gravitational waves originating from the direction (θ, ϕ, ψ), we use antenna patterns. It shows the sensitivity of the detector as a function of

the position of the event, and in our case the antenna pattern is defined by the two functions F_+ and $F_\times$ representing the sensitivity according to the plus and cross modes.

In the referential where the KAGRA detector is placed at $z = 0$ and its arms are along respectively x and y we get the figure 3.10. This figure show the sensitivity of KAGRA according to the angle of incidence of the gravitational wave. It can be seen that some areas are more sensitive than others, but that some areas are blind spots, such as the $x = y$ bisector, which can be explained by the fact that the gravitational wave will disturb both arms in the same way. This justifies the importance of having several detectors to cover all these shadow zones.

Figure 3.11 shows a signal from the O3GK dataset, corresponding to the difference between the length of each arms of the KAGRA detector. The data currently recorded by KAGRA comes from the O4 catalog and is still private to this day.

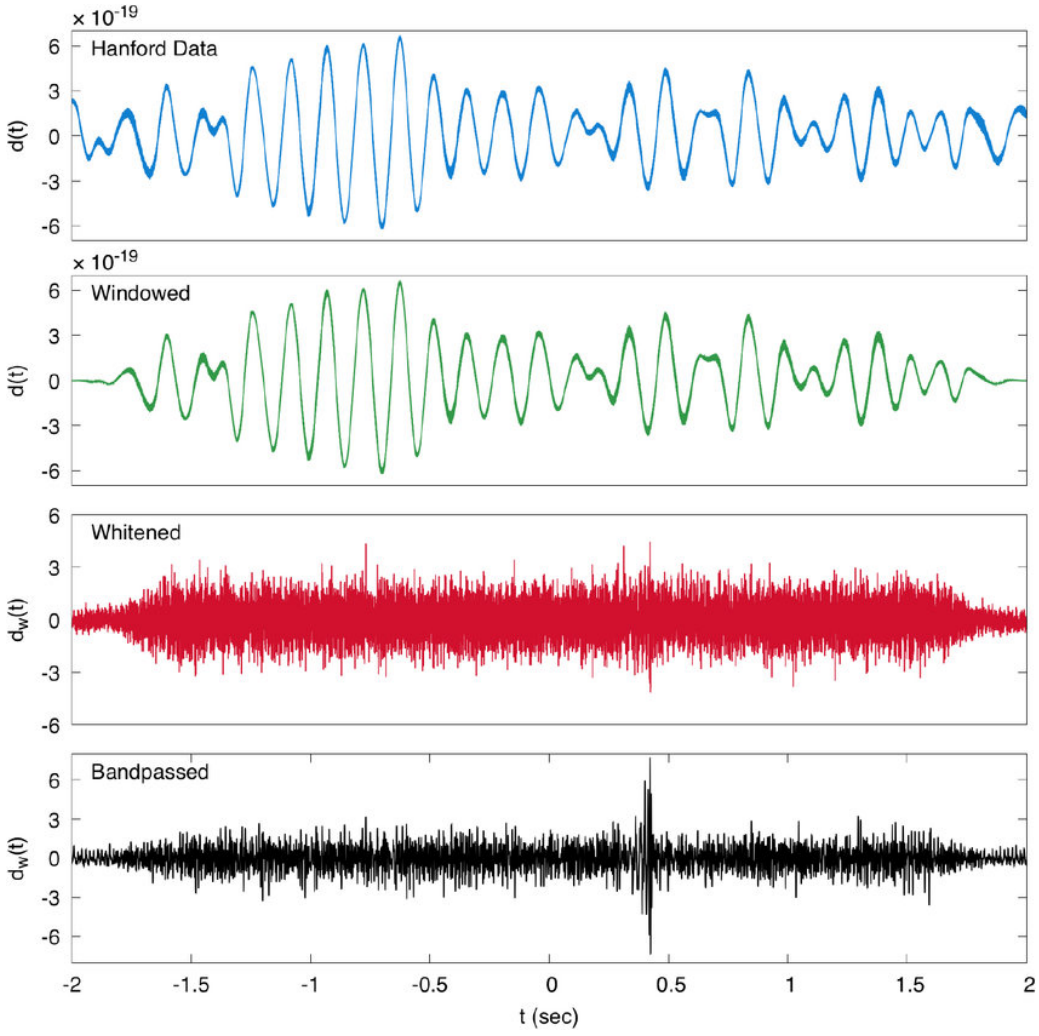

Figure 3.11: Example of a strain signal collected by Hanford with a gravitational wave incidence.

Since the gravitational wave has a lower amplitude, it is difficult to detect with a signal in this form. A shift to the frequency domain reveals the frequencies specific to the gravitational wave.

The signal sampling frequency is 16384 Hz (also denoted 16 kHz) and the order of magnitude of the strain is 10^{-14} in this very specific context of Observation #3 GEO-KAGRA (O3GK) run for KAGRA. The amplitude depends on the sensitivity of the detector, which is linked to the PSD.

A way to determine stationary noise is by computing its power spectral density (PSD). This is a mathematical representation of the power spectrum as a function of its frequency, and its formal definition is given by the Fourier transform of the frequency response function of a signal or random stationary process:

$$S_x(f) = \lim_{T\to\infty} \frac{1}{T} \left| \int_{-T/2}^{T/2} x(t) e^{-i2\pi f t} dt \right|^2 \tag{3.2}$$

In our case, we use the Welch approximation, which decomposes the signal into several overlapping windows and then performs a Fourier transform (FFT) on each window, taking the square of the absolute value and proceeding to the arithmetic mean. The figure 3.12 show this by taking an overlap of 50%. The choice of the number of windows is a crucial parameter in the PSD estimation: the more windows, the more noise will be averaged and the lower the frequency resolution.

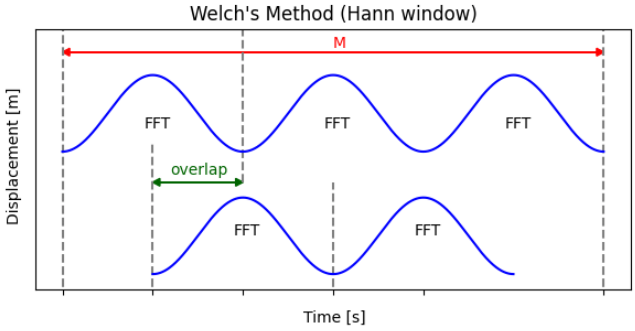

Figure 3.12: PSD Calculation using Welch's method

The advantage of the PSD is that it eliminates transient noise and allows to visualize the energy distribution of the signal with respect to frequency. It is more often convenient to display the logarithm of the PSD defined as:

$$S_{x,\mathrm{dB}}(f) = 10\log\left(\frac{S_x(f)}{I_0}\right) \tag{3.3}$$

With I_0 defined as an arbitrary reference, often the noise reference.

Amplitude spectral density (ASD) is commonly used in signal processing and is defined as the square root of the PSD:

$$\mathrm{ASD} = \sqrt{S_x(f)} \tag{3.4}$$

ASD can be easier to interpret than PSD, as it directly expresses the amplitude of oscillations or signals at different frequencies, rather than power (which is quadratic).

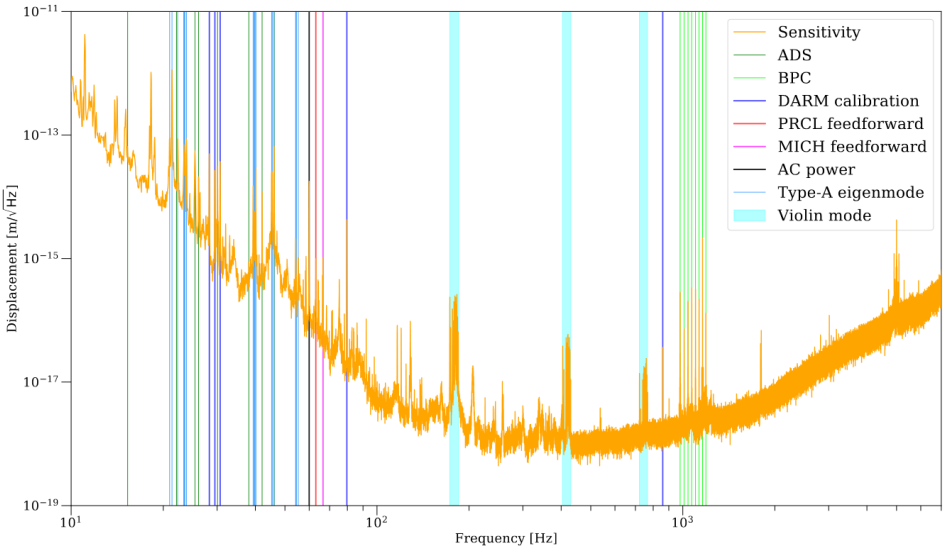

Figure 3.13: KAGRA's ASD

We can see three different regions in the ASD of KAGRA (Fig 3.13):

- The low-frequency region (before 100 Hz): Noise is relatively high at low frequencies, but decreases as frequencies increase.
- This middle-frequency region (between 100 Hz and 1000 Hz) which is flat in terms of spectrum, is of major interest for scientific analysis. However, peaks known as "Violin modes" can be observed in this portion, which are characteristic of the suspension's own modes of vibration. These peaks are particularly intense and can interfere with measurements. Bandpass filters are often applied to focus on the frequencies of interest.
- The high-frequency (above 1000 Hz): the PSD shows a marked increase. This rise is generally attributed to quantum effects.

The Signal-to-Noise Ratio (SNR) of a detector's datasteam is a statistic used to do match filtering. In this definition of SNR, we are looking for a model h. We are searching in the frequency domain, so we define $\tilde{h}$ as the Fourier Transform of h. Because we want to compare it with an other signal, we denote $tildeh^*$ as the complex conjugate of the Fourier transform.

The following method is defined in the book [9]. We assume that the model we're looking for (h) is embedded in the noise (n) of the received signal (s): $s(t) = h(t) + n(t)$. From the, PSD of the noise can express by the following formuula: $\langle \tilde{n}(f)\tilde{n}^*(f')\rangle \equiv \delta(f-f')S_n(f)$

$$(h|s) = \int_{-\infty}^{\infty} \frac{\tilde{h}^*(f)\tilde{s}(f)}{S_n(f)}\,df \tag{3.5}$$

The inner product described in equation 3.5 is then normalize by the inner product of the model h with himself. $(h|h)$ is used as normalization as this is optimal case where there is no noise ($s(t) = h(t)$). SNR can be higher than 1 if h is amplified (Amplitude measured in s is larger than the one in h). The final SNR is given by $\frac{(h|s)}{(h|h)}$.

This method is particularly effective for extracting weak signals embedded in noise. The scalar product weighs each frequency contribution of the signal against the noise $S_n(f)$, allowing frequencies where the noise is lower to contribute more to the SNR, maximizing the chances of detection, even in the presence of strong disturbances.

One of the major advantages of this method is that it exploits all available information on the spectral shape of the noise. By taking into account the PSD of the noise, this approach allows greater weight to be given to frequency bands where the disturbance signal is more significant and the noise is less.

3.2.4 Thermal suspension noise

The noise we're interested in is in the navy blue bands in the figure 3.7, corresponding to the suspension thermal noise. There are 3 blue band, corresponding to the mode of the violin noise and therefore, the first harmonic is the higher. The navy blue band is not only one peak, but a group of thirty peaks since the architecture of KAGRA is more complex that just one string. The noise is modeled as a damped harmonic oscillator. Although the detector has an relatively low ambient temperature, it is sufficient to generate thermal noise and makes the mirrors oscillate again. This model allows us to understand that this noise is not constant over time, and that it is therefore not possible to simply subtract the signal amplitude at this point.

The appropriate term for this noise is suspension thermal noise, because it comes from Brownian motion of particule hitting sapphire mirrors and others. These peaks are also called violin noise since they are from vibrations of strings. The aim is to suppress these peaks without compromising the information present in this frequency range, which prevents us from simply applying a notch filter.

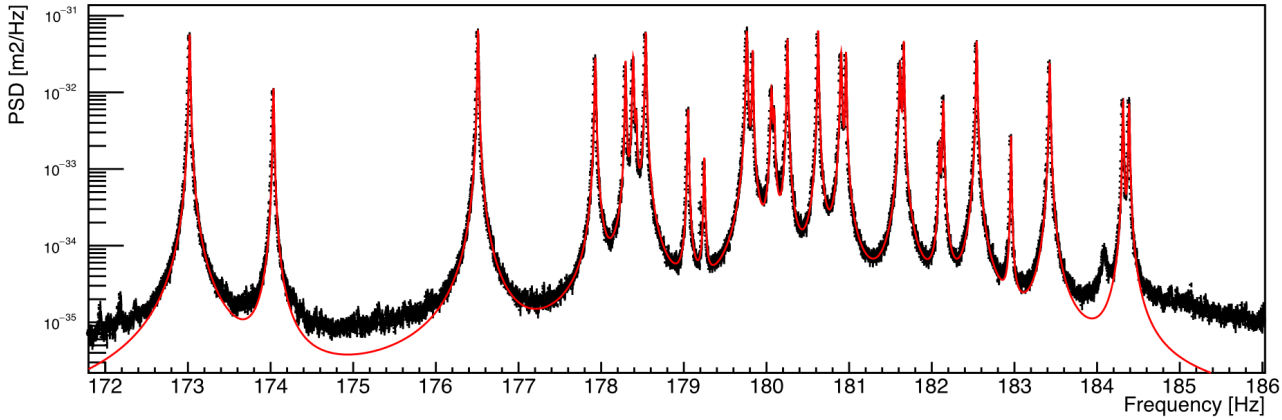

Figure 3.14: Focus on the KAGRA PSD area of interest

Note that the peaks have different amplitudes and widths (Fig 3.14), and can sometimes be located very close to each other. The aim is therefore to remove each of these peaks while creating the minimum possible loss of information in relation to the original signal.

3.3 First discoveries

Since the first observing run (O1), the gravitational wave community has progressively improved its sensitivity through successive observation runs, including O2 and O3. Each run has led to the detection of a growing number of gravitational wave events, ranging from black hole mergers to neutron star collisions.

A good way of visualizing gravitational waves incidence, and in general transient events, is the Q-transform. It is based on a time-frequency decomposition that uses windows whose width in the time domain and width in the frequency domain are related to each other in such a way that the greater the width of the time window, the smaller the width of the window in the frequency domain, and vice versa.

The q-transform optimizes the zones of interest to be more precise on certain frequencies with a non linear binning, while saving time by lowering the definition of uninteresting frequency zones [11]. We will now present two pioneering events in the discovery of gravitational waves.

3.3.1 Event GW150914

The first gravitational waves were detected on September 14, 2015 at 9:50:45 UTC during the O1 run and corresponded to the merger of two black holes, each around 30 times heavier, than our Sun at around 410 megaparsec, or more than a billion light-years away.

The figure 3.15 is composed of several sub-figures from top to bottom taken from the Hanford (on the left) and Livingston (on the right) LIGO detector. At the very top is a smaller replica of the figure 2.2. Using the signal, and the Q-transform graph, we can clearly see the three phase described in section 2.2, namely, the inspiral phase, where the signal gains in amplitude and the frequency is relatively low, the merger phase where the signal reaches its amplitude peak and has a very high frequency (we can notice a chirp on the Q-transforms on the last row of figure 3.15) and finally the ringdown phase, where the signal amplitude decreases and then disappears.

Despite being separated by several kilometers and after suppressing any potential correlated noise, both detectors measured a signal whose distribution matched the expected pattern of a gravitational wave generated by the merger of two black holes with masses M1 = 36 ($M_\odot$ and M2 = 29 with ($M_\odot$ representing the mass of the sun) [1]. This signal represents the first direct detection of a black hole binary merger. This discovery provided also the proof of the existence

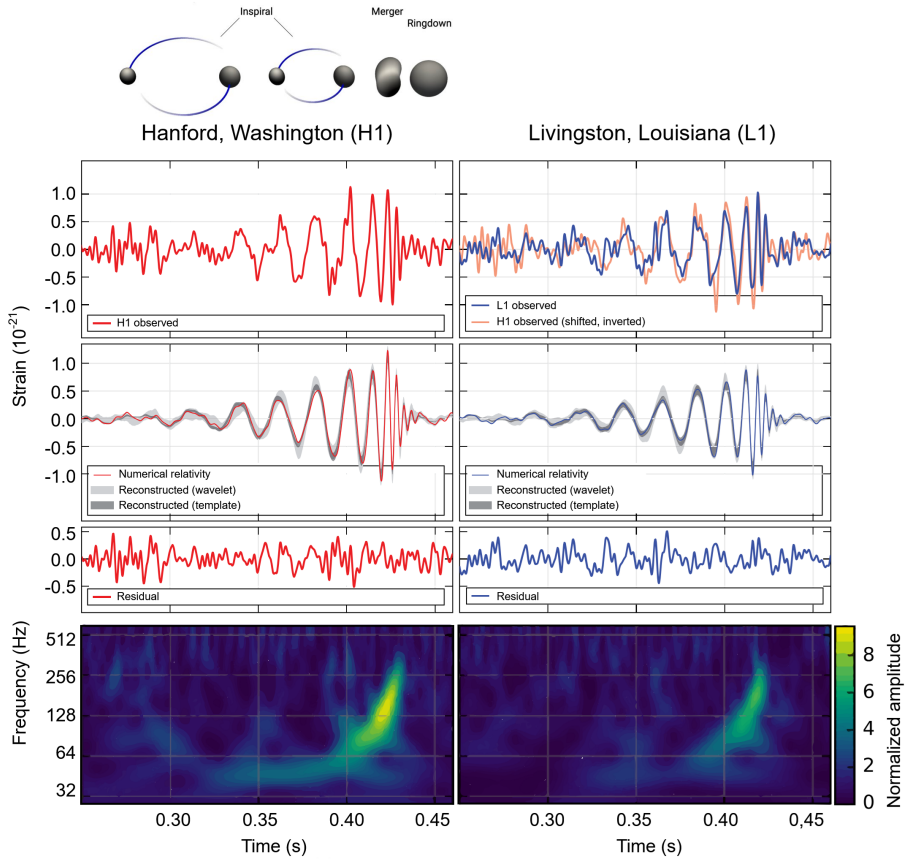

Figure 3.15: Signals picked up by LIGO detectors during event GW150914

of gravitational waves, marking in 2015 the beginning of a new era in astrophysics.

3.3.2 Event GW170817

Another important detection is GW170817, the first merger of a couple of neutron star on the 17th August 2017 at 12:41 UTC.

Unlike GW150914, which was detected solely by gravitational observatories, GW170817 was first observed by the Fermi GRB (Gamma-Ray Burst) telescope and the INTEGRAL telescope (cf fig 3.16), before being confirmed by LIGO and VIRGO. This type of event is particularly interesting because it represents a multi-messenger detection, combining the observation of gravitational waves with electromagnetic signals, providing a more complete view of astrophysical phenomena.

Although GW170817 was less intense than GW150914 in terms of gravitational wave amplitude, it was distinguished by its much longer duration. This event corresponds to the merger of two extremely dense neutron stars, in contrast to the black hole merger observed in GW150914. The coalescence of the neutron stars not only generated gravitational waves, but also produced a kilonova, an explosion ejecting materials rich in heavy elements such as gold and platinum. This process has led to a better understanding of the origin of these elements in the Universe, reinforcing the hypothesis that neutron star mergers are a major source of the creation of these elements in the cosmos.

By cross-referencing observations from different detectors, such as LIGO and Virgo, gravitational events can be pinpointed, as shown in figure 3.17. Each interferometer measures differences in wave arrival times, narrowing down the likely region on the sky. Thanks to triangulation, the area has been greatly reduced. The optical telescopes, pointed at this region, then detected the electromagnetic counterpart, enabling a very precise localization of the source, illustrating the effectiveness of the multi-messenger approach.

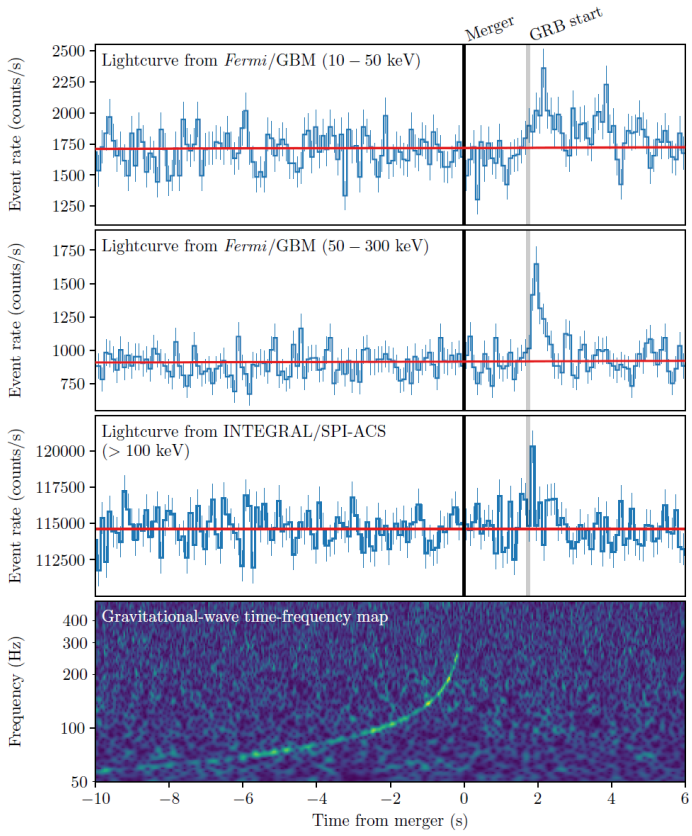

Figure 3.16: Detection of the GW170817 event by several detectors

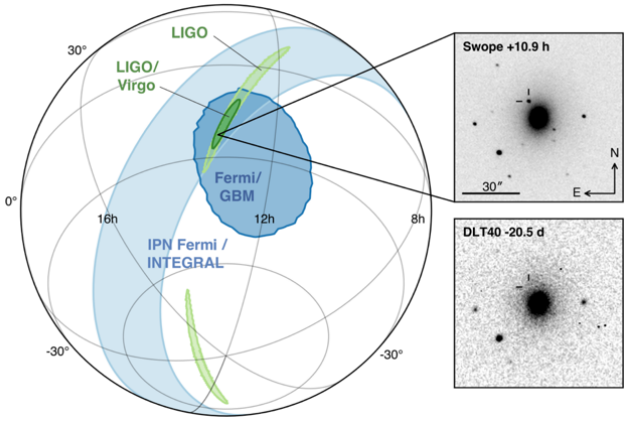

Figure 3.17: Sky map of the GW170817 event

GW170817 also marks the start of a new multi-messenger era, in which gravitational waves are detected in parallel with other types of signal, such as gamma-ray bursts. This ability to observe the same astrophysical events with different types of messenger opens the way to unprecedented discoveries in the physics of neutron stars and gamma-ray bursts. These multi-messenger observations make it possible to constrain more astrophysical parameters, such as the equation of state of neutron stars, and refine our understanding of violent phenomena occurring in the Universe.

Today, the LVK (LIGO-Virgo-KAGRA) collaboration detects several gravitational waves a week, with events ranging from stellar black hole mergers to neutron star coalescences. However, only two neutron star pair mergers have been detected since 2015, as they are lighter than black holes and therefore more difficult to detect.

4 Data Processing by Machine Learning

4.1 Architecture

SciNet is a model released in 2020 in the article *SCINet: Time Series Modeling and Forecasting with Sample Convolution and Interaction* [8]. SCINet stands out for its ability to capture temporal dependencies at different scales. By breaking down the data into smaller segments, the model is able to analyze short- and long-term relationships in greater detail. This method enables the model to better identify complex patterns in time series, while taking into account interactions between different data in a flexible way.

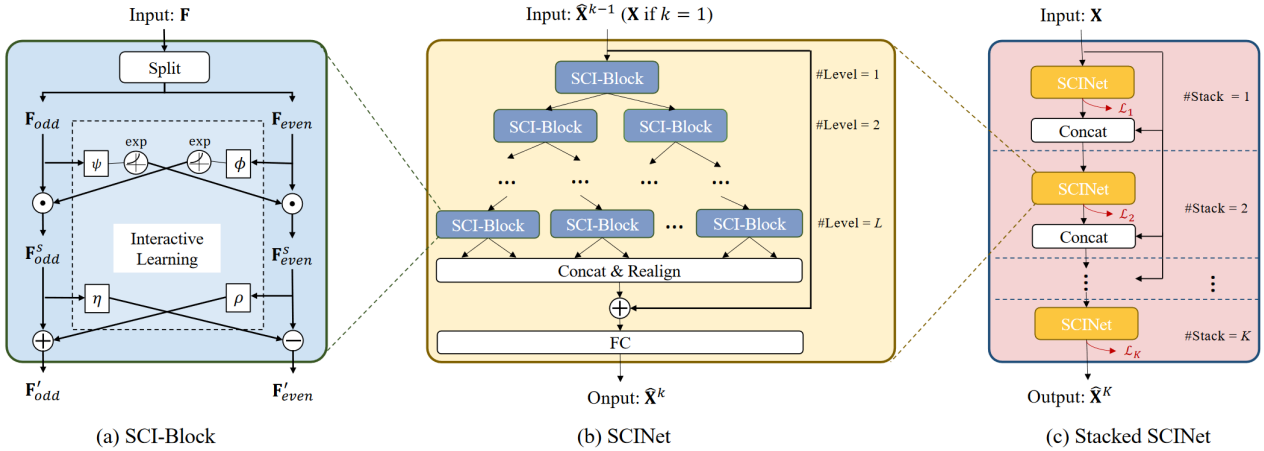

(a) SCI-Block (b) SCINet (c) Stacked SCINet

Figure 4.1: Scinet Model

This makes it more effective than conventional techniques such as ARIMA models or recurrent neural networks (RNN), offering more reliable forecasts, particularly in situations where several variables evolve together over long periods.

In our case, we want to use SCINet to try and predict the signal after it has passed through the interferometer. The aim is to try to recreate the signal without the various noise violin peaks. SCINet's architecture is shown in figure 4.1. It is divided into three parts:

4.1.1 SCI-Block (a)

The first part, on the left, describes an SCI-Block, a processing block in the SCINet architecture. The input, denoted F, is first divided into two sub-parts, F_{odd} and F_{even}, representing odd and even elements respectively.

Distinct convolution kernels, ϕ and ψ, are applied to F_{even} and F_{odd} respectively to extract unique features. To address potential information loss caused by downsampling, a new interactive learning approach is introduced. It enables the exchange of information between the two sub-sequences by having them learn affine transformation parameters from one another.

First, the sequences F_{even} and F_{odd} are projected into hidden states using two distinct convolutions, ϕ and ψ. These projections then interact via a Hadamard product to perform reciprocal subsequence scaling:

$$F^s_{odd} = F_{odd} \odot \exp(\phi(F_{even})), \quad F^s_{even} = F_{even} \odot \exp(\psi(F_{odd})).$$

This can be interpreted as applying scaling transformations to F_{even} and F_{odd}, with the scaling factors being learned from each other through neural network modules.

Secondly, the scaled features, F^s_{odd} and F^s_{even}, are projected into additional hidden states using two additional convolutions, ρ and η. These new features are then added to or subtracted from the scaled sequences:

$$F'_{odd} = F^s_{odd} \pm \rho(F^s_{even}), \quad F'_{even} = F^s_{even} \pm \eta(F^s_{odd}).$$

The different convolution kernels ϕ, ψ, ρ and η correspond to a set hyper-parameters of the model.

This approach improves information extraction by limiting losses due to downsampling. Downsampled sequences exchange transformations, which reinforces interactions between data and enables better capture of important dependencies, guaranteeing richer and more accurate interpretation of information.

4.1.2 SCINet (b)

In the SCINet structure, several SCI-Blocks are organized hierarchically to form a tree-structured framework. There are 2^l SCI-Blocks at level l, where $l = 1, \ldots, L$ represents the level index, and L is the total number of levels. Within the k-th SCINet, the input time series X (for $k = 1$) or feature vector $\hat{X}_{k-1} = \hat{x}^1_{k-1}, \ldots, \hat{x}^\tau_{k-1}\}$ (for $k > 1$) is progressively subsampled and processed by SCI-Blocks across different levels. This enables features to be extracted at different temporal resolutions.

After traversing L levels of SCI-Blocks, the elements of all sub-features are rearranged by reversing the odd-even separation operation and concatenated into a new sequence. This sequence is added to the original time series via a residual connection to generate a new sequence with improved predictive capability. Finally, a simple fully-connected network is used to decode this new representation into $\hat{X}_k = \{\hat{x}^1_k, \ldots, \hat{x}^\tau_k\}$.

4.1.3 Stacked SCINet (c)

In a Stacked SCINet, K layers of SCINets can be superimposed to further improve forecast accuracy, provided there are sufficient training samples, although this leads to increased model complexity.

To facilitate learning of intermediate temporal characteristics, intermediate supervision is applied using actual values on the output of each SCINet. The output of the kth intermediate SCINet, $\hat{X}_k$, of length τ, is concatenated with part of the input $X_{t-(T-\tau)+1:t}$ to recover the original length of the input, then used as the input of the next SCINet. This process continues until the last SCINet, whose output $\hat{X}_K$ is the final prediction.

4.2 Strain dataset generation and conditioning

The aim is to generate various time signals containing a violin peak at a given frequency. We also want to have control over the amplitude and width of the peak, so as to be able to train the SCINet neural network on a dataset whose components we have full control over. To do this, we're going to build on the method implemented in the article *Data conditioning for gravitational wave detectors: A Kalman filter for regressing suspension violin modes* [5].

The dataset is made up of the model's input data and the output data the model tries to approximate. The latter is called ground truth.

A violin peak is modeled as a damped harmonic oscillator, whose u coordinate represents the amplitude of a violin peak present in the detector output. The u coordinate obeys the following differential equation:

$$\ddot{u} + \frac{\omega_0}{Q}\dot{u} + \omega_0^2 u = F, \tag{4.1}$$

where:

- Q is the quality factor of the oscillator
- ω_0 is the proper frequency of the oscillator
- F is the (stochastic) driving force.

By noting $omega_c$ the peak pulsation, we can introduce the quantity $\psi = u\exp(-i\omega_c t)$., ruled by the following differential equation

$$\dot{\psi} + \left(\frac{\omega_0}{Q} + 2i\omega_c\right)\psi + \left(\omega_0^2 - \omega_c^2 + i\frac{\omega_c\omega_0}{Q}\right)\psi = F\exp(-i\omega_c t). \tag{4.2}$$

or, in the Laplace domain,

$$(s-p_+)(s-p_-)\tilde{\psi}(s) = \tilde{F}(s+i\omega_c). \tag{4.3}$$

with:

$$\tilde{g}(s) = \int_0^\infty \exp(-st)g(t)\,dt \tag{4.4}$$

$$p_\pm = -\frac{\omega_0}{2Q} - i\omega_c \pm i\omega_0\sqrt{1-\frac{1}{4Q^2}} \tag{4.5}$$

The two poles $p_\pm$ in the Laplace transform solution correspond to the positive and negative frequency resonances of the oscillator. By chosing ω_c close to ω_0, we can place ourselves in the s case close to p_+ and push p_- to infinity, which gives us a single peak.

$$(s-p_+)\tilde{\psi}(s) = \frac{\tilde{F}(s+i\omega_c)}{s-p_-} \tag{4.6}$$

for $|s| \ll |p_-|$ it becomes:

$$(s-p_+)\tilde{\psi}(s) = -p_-^{-1}\tilde{F}(s+i\omega_c) \tag{4.7}$$

This allows us to simulate a single peak instead of two.

To switch from an analog to a digital filter, we use the bilinear transform defined as follows (with $T = \frac{1}{f_s}$, the inverse of the sampling frequency) :

$$H_d(z) = H_a(s)\Big|_{s=\frac{2}{T}\frac{z-1}{z+1}} = H_a\left(\frac{2}{T}\frac{z-1}{z+1}\right) \tag{4.8}$$

For the dumped oscillator, this gives:

$$\begin{aligned} H_d(z) &= H_a\left(\frac{1-z^{-1}}{1+z^{-1}}\right) && (4.9)\\ &= \left[\frac{4}{T^2}\frac{z^{-2}-2z^{-1}+1}{(1+z)^{-2}} + \frac{2\omega_0}{TQ}\frac{1-z^{-1}}{1+z^{-1}} + \omega_0^2\right] && (4.10)\\ &= \frac{T^2Qz^{-2}+2T^2Qz^{-1}+T^2Q}{z^{-2}[4Q-2T\omega_0+T^2Q\omega_0^2]+z^{-1}[-8Q+2T^2Q\omega_0^2]+[4Q+2T\omega_0T^2Qw_0^2]} && (4.11)\\ &= \frac{\sum_{j=0}^{2} b[j]z^{-j}}{1+\sum_{j=1}^{2} a[j]z^{-j}} && (4.12) \end{aligned}$$

Given a pseudo-random process $F[k]$ and the recursive relation defined earlier with the coefficients $a[k]$, $b[k]$, we calculate $u[k]$, which represents the simulated contribution of the violin mode to the detector's output.

$$u[k] = \sum_{j=0}^{2} b[j]F[k-j] - \sum_{j=1}^{2} a[j]u[k-j], \tag{4.13}$$

To generate the signal containing the violin peak, we first define a reduced centered Gaussian noise that will serve as the basis for the peak, and whose mean will be used to define the PSD reference frame. From another reduced centered Gaussian noise, we'll generate the signal containing the violin peak, which we'll add to the base noise.

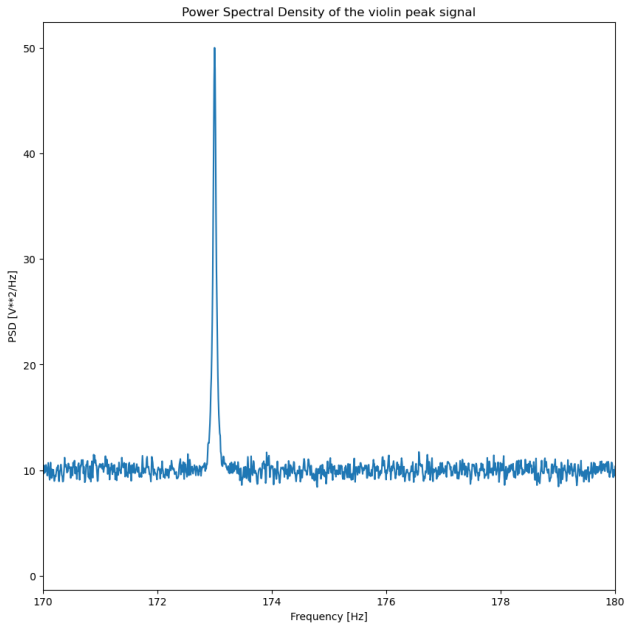

Figure 4.2: Base noise + violin peak PSD

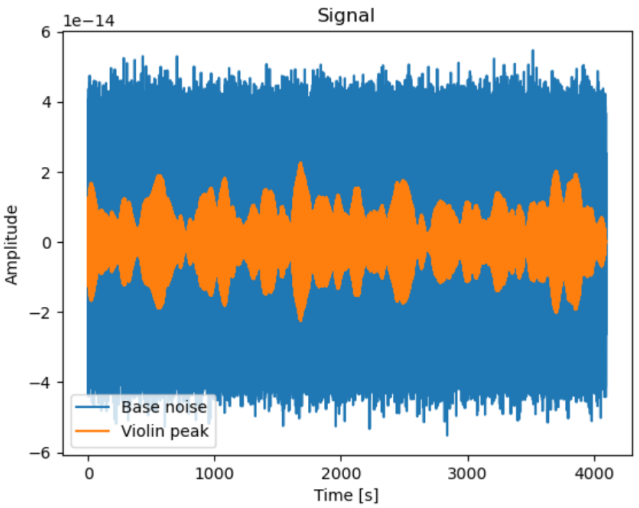

Figure 4.3: Superposition of Base noise and violin peak on time domain

The desired frequency of the peak corresponds to the first peak on the figure 3.14, i.e. 173 Hz. Figure 4.2 represent the PSD of the basic noise with and without the violin peak. The peak (that we might call suspension thermal noise, violin peak or even violin noise from now on) is well located at the desired frequency, with a definition of 0.03 Hz. The figure 4.3 shows the temporal representation of the basic noise and the signal containing only the peak. Firstly, the signal containing the noise is of greater amplitude than the violin peak, which is similar to the 3.11 in the sense that the violin noise should not be prominent on the signal in terms of amplitude.

In order to achieve the same conditions as for KAGRA, we use a signal sampled at $f_s = 16\,\text{kHz}$. The problem is that we're trying to suppress a frequency at 173 Hz, and using a signal with too high a sampling frequency only risks altering the data at frequencies beyond 173 Hz. To describe this maximum frequency, we use the Nyquist frequency F_N defined as:

$$F_N = \frac{f_s}{2} \tag{4.14}$$

The Nyquist frequency is used to define the maximum frequency (F_n) that a signal must contain to enable it to be described unambiguously by sampling at regular intervals at a sampling frequency f_s. We decided to decimate the signal, i.e. downsample and then apply an anti-aliasing filter, at 2kHz (2048Hz) because, even if the first peak is still at 173 Hz the third harmonics are around 800Hz and we want the method to be any peak of any harmonics.

Another objective is to implement the SCINet model on the KAGRA livestream (with is sampled at 16384Hz), which updates every second, so we've tried to work with signals of more than one second at most. As a result, the dataset used as input data for SCINet is made up of signals sampled at 2kHz, whose temporal duration has yet to be determined, comprising base noise, a reduced-centered Gaussian noise, plus violin noise at 173 Hz. The comparison data, the ground truth, is the same signal, but without the violin noise.

At this stage, the notion of noise refers to the gaussian with a 10 dB amplitude in figure 4.2 and signal noise refers to the violin peak (Fig 4.2), although in KAGRA both are considered noise. Therefore, the main goal now is to reduce the signal (the peak) over the base noise.

4.3 Loss function

Originally, SCINet was used for time-series prediction. That's why, in their article [8], the authors choose the input window size as drastically larger than the output size, because the aim is to predict future values. In our case, if the input signal is larger than the output signal, then there would be a loss of information due to the reduction in signal duration, and if the output signal was larger, then there would be an extrapolation of the signal beyond one second, which is not what we want. Moreover, to compare the two signals, it is easier if they are the same size. That is why we've chosen the same size for the entry and output signal.

The STFT equation for a signal x is given by:

$$\mathrm{STFT}\{x\}(\tau,\xi) = \int_{-\infty}^{\infty} x(t)\, w(t-\tau) e^{-i2\pi\xi t}\, \mathrm{d}t \tag{4.15}$$

For the discrete STFT, the result is a two-dimensional array containing:

- On each line: the variation in intensity of a given frequency over time
- On each column: a Fourier transform of the window in question

Like the Fourier transform, STFT is a complex signal. To facilitate visualization, we use the spectrogram defined as square the absolute value of the STFT:

$$\mathrm{Spectrogram}\{x\}(m,\xi) = |\mathrm{STFT}\{x\}(m,\xi)|^2 \tag{4.16}$$

To define the loss function, we calculate the STFT of the input signal and the output signal. Since STFT is a complex two-dimensional signal, this means controlling the evolution of the phase and modules of the transform over time which are represented in figures 4.4 and 4.5.

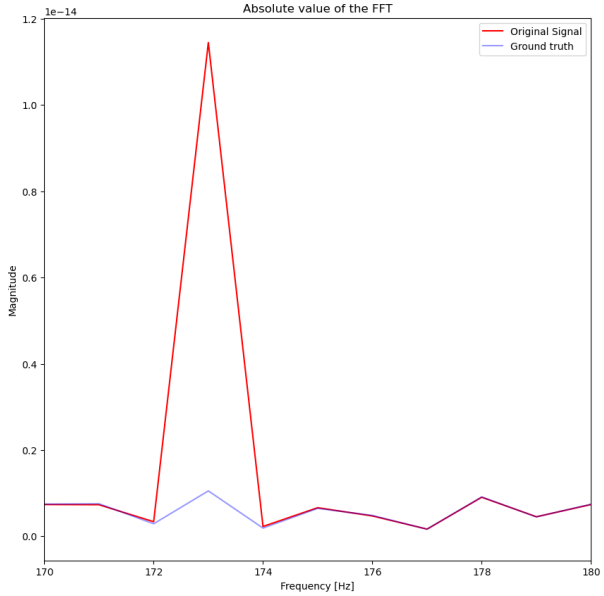

Figure 4.4: Absolute value of the FFT

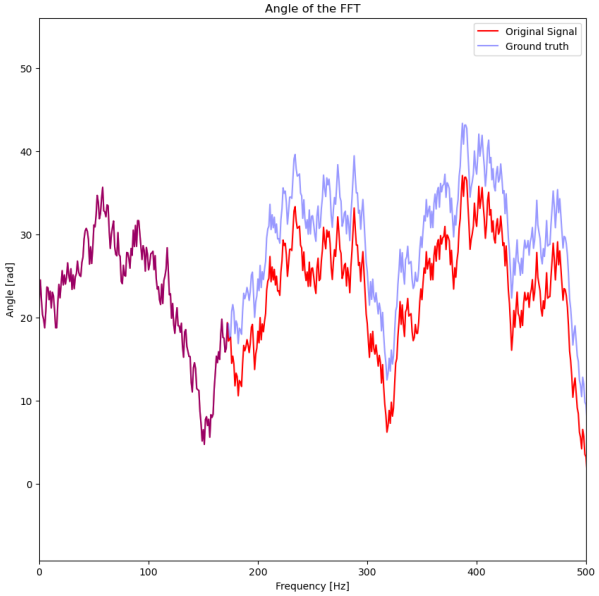

Figure 4.5: Angle of the FFT

Differentiating these two STFT gives us our loss function (with τ the length of the signal):

$$\mathcal{L}(x,y) = \frac{1}{\tau} \sum_{f=1}^{F_N} \sum_{t=1}^{T} \left| \mathrm{STFT}_x(f,t) - \mathrm{STFT}_y(f,t) \right| \tag{4.17}$$

If the number of stacks in SCINet is equal to $k > 1$, we define the loss function as the sum of the loss function at each layer :

$$\mathcal{L}(x,y) = \sum_{k=1}^{K} \mathcal{L}_k. \tag{4.18}$$

This approach has numerous advantages comparing others:

- Compared to the signal comparison as such: this accentuates the comparison on the violin peak, which is not identifiable as such on the signal.
- Compared to the Fourier transform: This allows us to see the SCINet effect over time, unlike the Fourier transform, which gives the frequency peak over one second of signal. We could have partial false corrections on parts of the signal that cancel out over the whole duration.
- Compared to the study of the peak at the given frequency: this prevents the system from focusing exclusively on the peak and affecting other frequencies. We want the system to reduce the peak, but we don't want the other frequencies to change, as this would create noise that we wouldn't be able to model and interpret.

This method can only be used to compare signals of the same length and sampling frequency f_s, which is not a problem in our case, given the measures taken.

4.4 Model training

To avoid having to handle quantities that are too small and therefore having huge weights, the input signal is renormalized by dividing it by the noise standard deviation, allowing us to work with values of the order of unity.

We split a 70%, 30% between training and test data. We trained the model with a dataset containing $T = 500,000$ bins (≈ 244 seconds). The signals from all τ bins are subsamples of the form $x[t, t+\tau]$ with $t \in [0, T-\tau]$ with T the length of the dataset. We split a 70%- 30%, between training and test data. A batch size of 16 was used, along with a decreasing learning rate of 0.009.

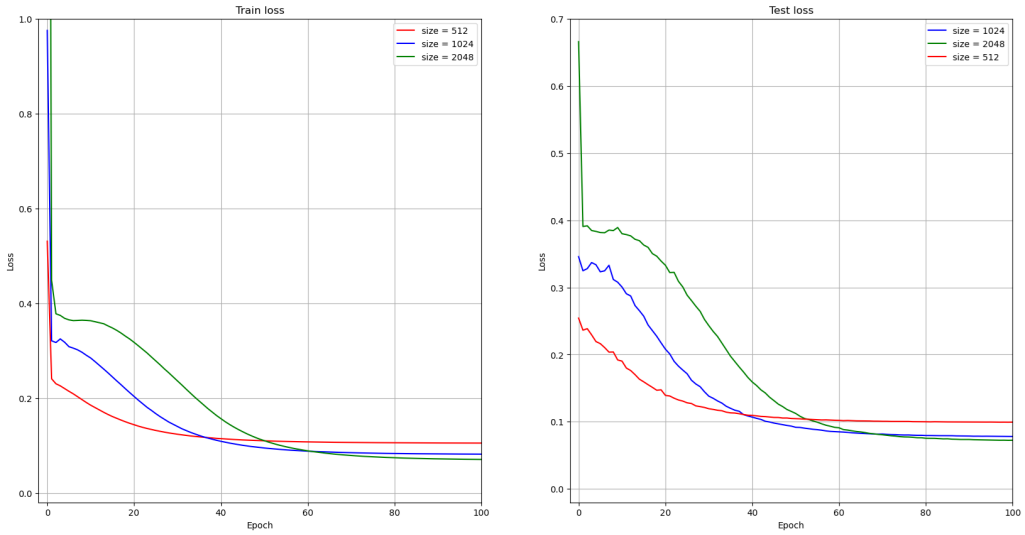

Figure 4.6: Performance comparison by signal length

For model hyper-parameters, there are:

- The size of the signal, and therefore the number of SCINet input pins. This is the first hyper-parameter we wanted to deal with, to see if there was any interest in taking a larger signal, and therefore having a higher computational cost. Figure 4.6 shows the variations in training and test errors over the epochs. We can see that size does indeed influence the loss function, and that after a certain number of epochs, a larger size brings a better test error.
- The size of the kernel k of convolutions ϕ, ψ, ρ, η in SCI-block defined in the Section 4.1.1.
- The number of level in the SCINet structure in every SCINet, defined in Section 4.1.2.
- The number of stacks defined of the stacked SCINet structure, defined in Section 4.1.3.

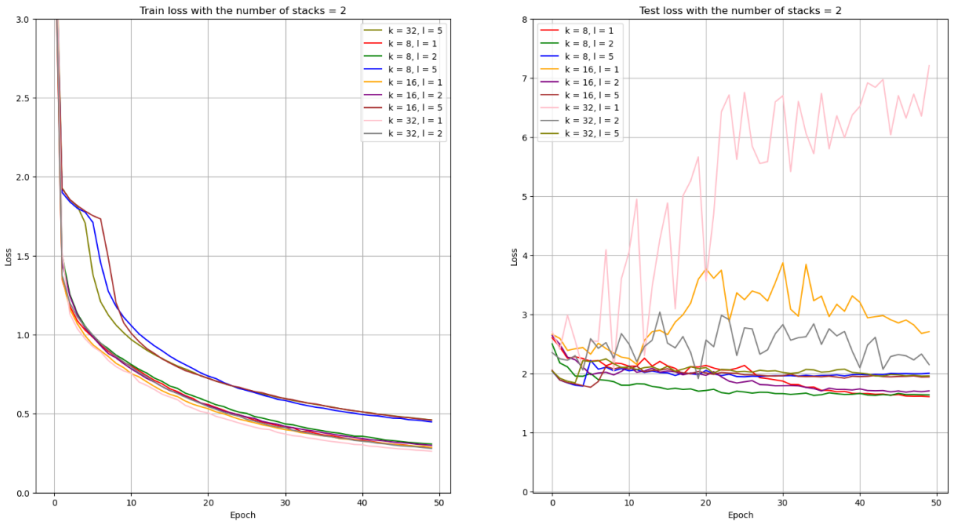

Figure 4.7: Performance comparison when the number of stacks is equal to 2

Figure 4.7 highlights overfitting when stacking SCINet models. This can be explained by the fact that, after the first SCINet, the output signal becomes the input signal for the second SCINet which leads to the application of a new SCINet on an extrapolated signal. Initially, this stacked SCINet model is useful for short-term prediction, taking long input signals to predict small output signals. This made it possible to have an input signal composed mainly of real data for stacked models.

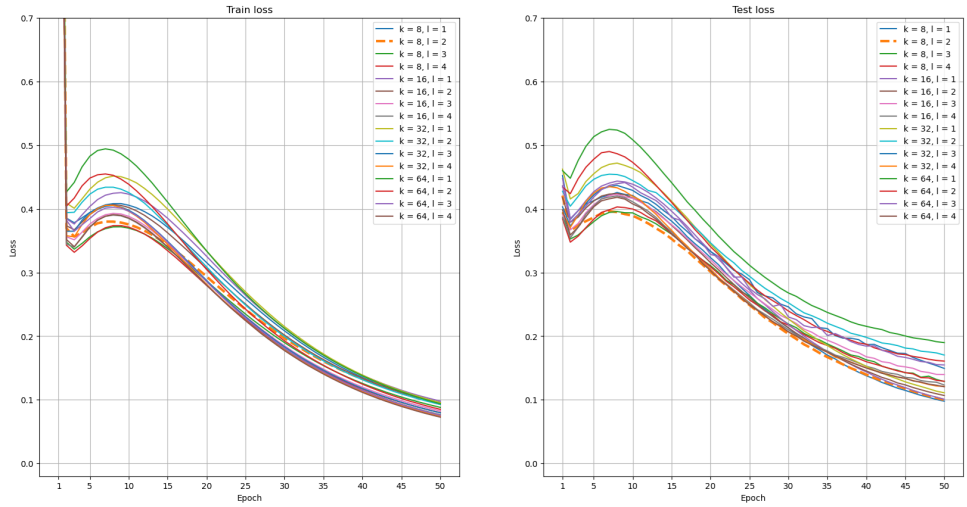

Figure 4.8: Performance comparison with different kernel size k and number of layer l

We tried different core sizes and different numbers of layers to find the best model. We trained different models as shown in figure 4.8. These hyper-parameters play minor role in the results of the test function as we can see the same behavior for every curve and similar results. We kept the model that gave us the best results after 50 epochs, i.e. a kernel size of 8 and a number of layers of 2 represented by the large orange dotted line.

We then train the chosen model over a larger number of epochs (200), and the model converges after around 100 epochs, as seen in figure 4.9. In this sub-section, all results will be produced by this model unless otherwise indicated.

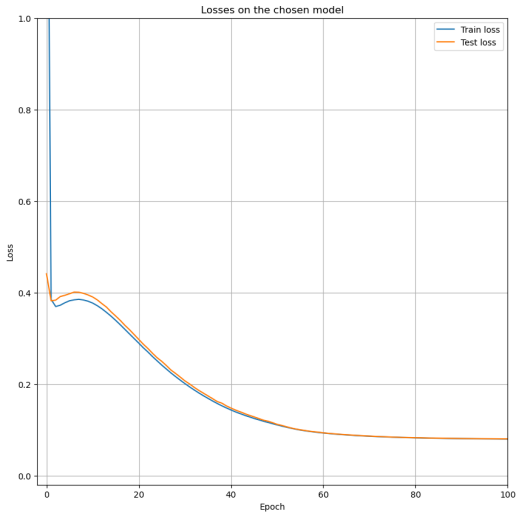

Figure 4.9: The number of layer is 2, kernel size is equal to 8 and there in only 1 stack of SCINet model

5 Suspension Thermal Noise Reduction

5.1 One peak suppression

In this section we'll focus in more detail on the effect of SCINet on peak suppression. As mentioned above, we've used the Short Time Fourier Transform, but to compare signal pairs in more detail, we'll look at the signal-to-noise ratio (SNR) defined as follows in the section 3.2.3. We replace the noise PSD by the signal's Gaussian noise, and the template by the violin peak signal at 173 Hz (without base noise).

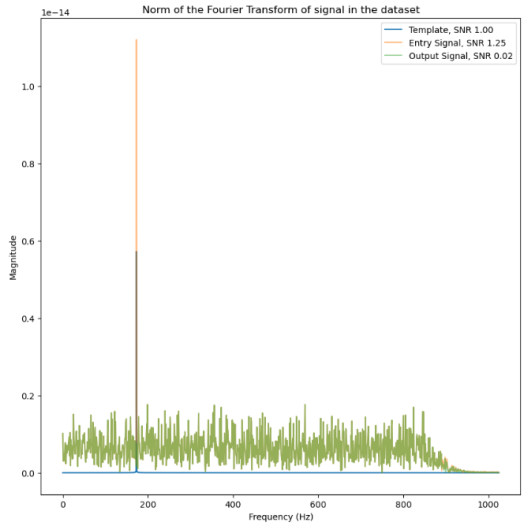

Figure 5.1: Example of SNR Calculation by plotting the norm of Fourier Transforms

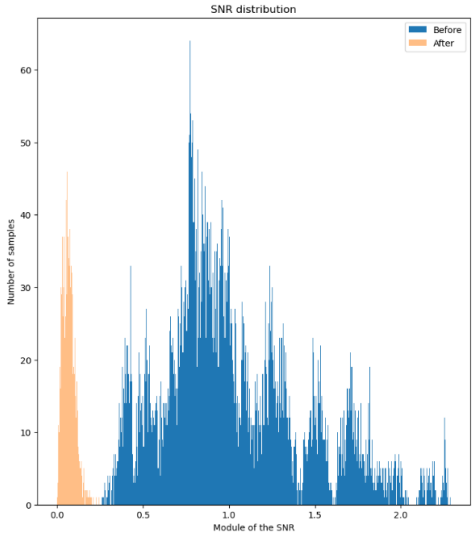

Figure 5.2: SNR Distribution before/after SCINet

Figure 5.10 highlights the impact of SCINet on the Signal-to-Noise Ratio (SNR), specifically focusing on the reduction of suspension thermal noise within the dataset. The SNR distribution clearly shows a significant shift before and after the application of SCINet, with the orange distribution representing the post-SCINet SNR values being much lower than the blue distribution representing the initial SNR values. This reduction indicates a successful mitigation of the thermal noise, which is characterized by high SNR peaks that can obscure the underlying signal of interest.

To analyse a signal longer than one second, we split a 50-seconds signal into 50 samples, each of which we then ran through SCINet before reconstructing the signal by concatenating each of the sub-signals.

This step-by-step reconstruction allows for a precise observation of how SCINet processes each segment, and in turn, how the model reconstructs the overall signal.

The main objective of applying SCINet in this context is to attenuate the suspension thermal noise, which is known to contribute intensely to the overall noise within the data. This noise appears as sharp and prominent peaks in the Fourier spectrum (see Figure 5.10), complicating the interpretation of the signal. By using SCINet, these peaks are effectively reduced, resulting in a much flatter SNR distribution and hence a cleaner signal.

The absence of outliers in the post-SCINet distribution is crucial, as it indicates that SCINet not only reduces the overall noise levels but does so consistently across different segments of the data. To better understand the efficiency of SCINet, a single random signal from the dataset will be used as an example.

To better analyze the influence of SCINet for the suspension reduction, we have shown in figure 5.3 the absolute value of the Fourier Transform of the input signal, the suspension reduction signal, as well as the ground truth and the difference between the model output and this ground truth, each with a 50 seconds length. These visualizations highlight the effects of the model on the processed signal.

The first line, corresponding to the FFT graphs, is the evolution of the peak at 173 Hz. This peak is clearly attenuated by SCINet. The desired effect is achieved: no other unwanted frequencies appear under the effect of SCINet, indicating

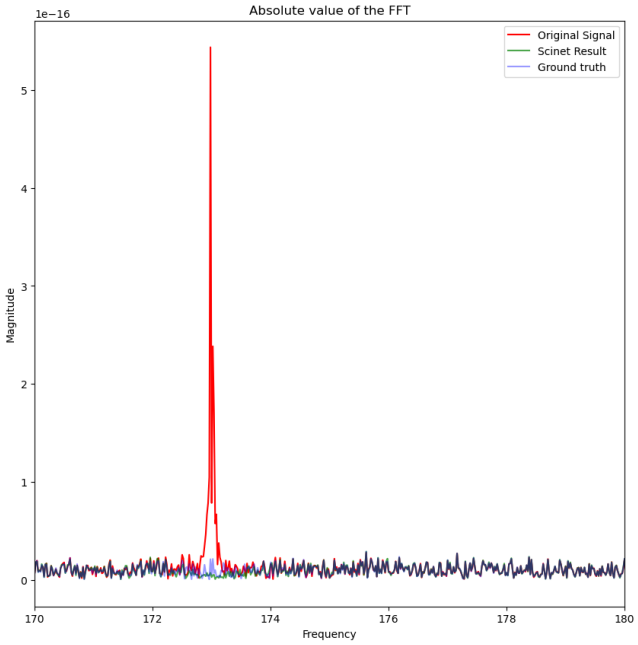

Figure 5.3: FFT Absolute value of the entry signal, the output, the ground truth

that the model is able to effectively target a specific frequency while preserving the other frequency components of the signal.

The figure 5.3 also reveals that no additional peaks were generated at frequencies other than 173 Hz since the suspension reduction signal overlaps the entry signal, confirming that the model has indeed modified only the desired frequency component. However, one problem persists, we can see that there is some residual. By looking closely at the second and third plots, we notice that the suspension peak is overcorrected. Instead of corresponding to the ground truth, the frequency component at 173 Hz is reduced to almost zero, which was not the desired effect. There are also slight fluctuations in the surrounding frequencies, but of relatively low amplitude. This indicates that SCINet could sometimes apply too drastic a correction to certain frequencies, requiring adjustment so as not to degrade non-target frequencies.

This result highlights both SCINet's strength in effectively targeting specific frequencies such as 173 Hz, but also its limitations in correction dosage. To improve performance, it might be necessary to introduce a regulation mechanism or additional filtering to limit the amount of reduction applied. The drastic reduction of SNR across the peaks confirms that SCINet consistently suppresses the suspension thermal noise. Consequently, this example reflects the general effect of SCINet on the dataset as a whole, leading to a substantial improvement in the signal quality by significantly reducing the thermal noise that would otherwise dominate the signal spectrum.

5.2 Two peak suppression

As part of this study, we set out to evaluate the influence of SCINet on two sufficiently close peaks, in order to understand the potential impact of the model when applied to neighboring frequencies. To do this, we selected the second peak in KAGRA's PSD visible in figure 3.14, which lies at around 174 Hz. This exercise is particularly relevant because SCINet is designed to effectively suppress frequency peaks and adjacent bands around these peaks, even when the peaks are thin. However, when it comes to peaks that are sufficiently close together, a problem can arise: the model risks not only suppressing the targeted peaks, but also affecting their spectral neighborhoods, thus generating unexpected disturbances in the intersection of neighborhood zones.

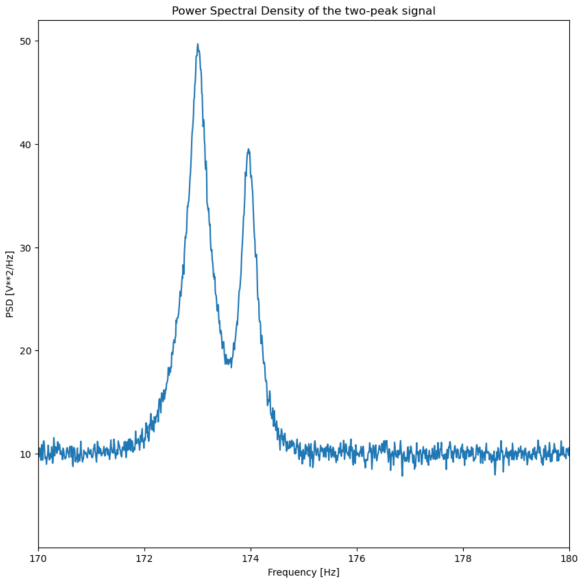

Figure 5.4: PSD of the 2-peak signal

The figure 5.4, corresponding to the image presented here, clearly illustrates this phenomenon with two closely spaced peaks at around 173 Hz and 174 Hz. The aim is to check whether SCINet can handle such cases accurately without introducing major distortions in the surrounding frequencies or causing excessive suppression of the frequency bands between the two peaks. To avoid affecting the intermediate region between the two peaks, we apply SCINet to these two peaks in sufficiently close proximity, while carefully monitoring the model's response in this critical area.

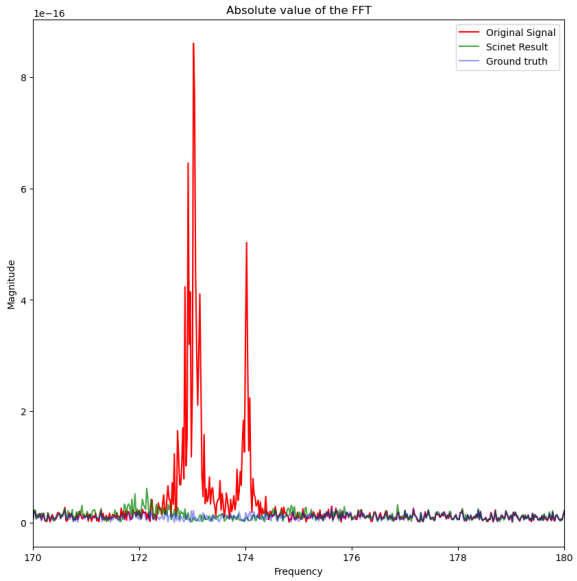

Figure 5.5: FFT Absolute value of the entry signal, the output, the ground truth

Figure 5.5 corresponds to the magnitude of the Fourier transforms for a signal with two overlapping peaks. As in the previous section, once the signal is segmented, each piece is individually passed through the SCINet model to handle the 173Hz and 174Hz peaks. After that, we can reconstruct the initial signal and see its properties

First of all, we notice that the two peaks have been considerably reduced, as has the area of intersection between them. However, we note that the signal suspension reduction presents small peaks at around 172 Hz, demonstrating SCINet's difficulty in processing overly complex signals.

Such modifications may seem insignificant, but given that the aim is to apply SCINet to the signal several times, they could lead to propagation errors, which should be avoided at all costs, given that there are around 30 peaks per harmonic. Given that the signal is more complex, a more complex model might have been more appropriate, by repeating the procedure used to select the 1 peak system, but for lack of time we were unable to do so.

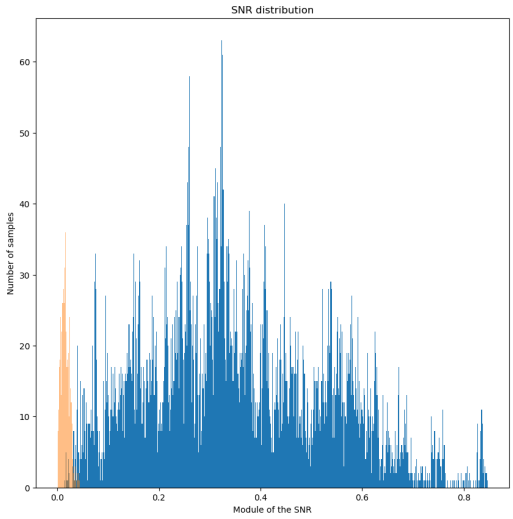

Figure 5.6: SNR Distribution before/after SCINet

Looking at the SNR distribution before and after suspension reduction, we can see that there is still a drastic reduction of the SNR, as in the previous section. It's important to note that the SNR scale is not the same as in figure 5.10, which is due to the fact that the presence of two peaks pulls this SNR downwards.

We obtain the same characteristics as in section 5.1, i.e. a reduction of the signals and, in this case, of the two peaks, as well as an absence of outliers in the final distribution, which means that the model has reduced all the thermal suspension noise on all the signals, whatever the peak intensity. Although it added more noise, the more complex pattern of the peak was deciphered by SCINet, which was able to reduce the SNR.

5.3 Gravitational waves incidence

To generate a gravitational wave, we'll use GW150914's gravitational wave template to which we'll add the base noise and the violin peak at 173Hz, to give figure 5.7.

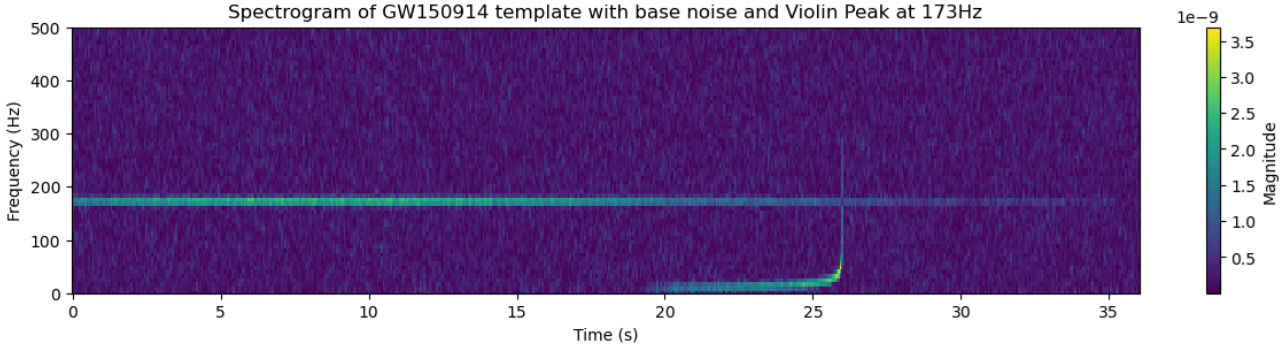

Figure 5.7: Template of GW150914 + base noise + violin peak

When we look at the peak in the Fourier transform (cf Fig 5.8), it has been suppressed as before and the rest of the signal has been preserved, whether at 173 Hz or at more distant frequencies.

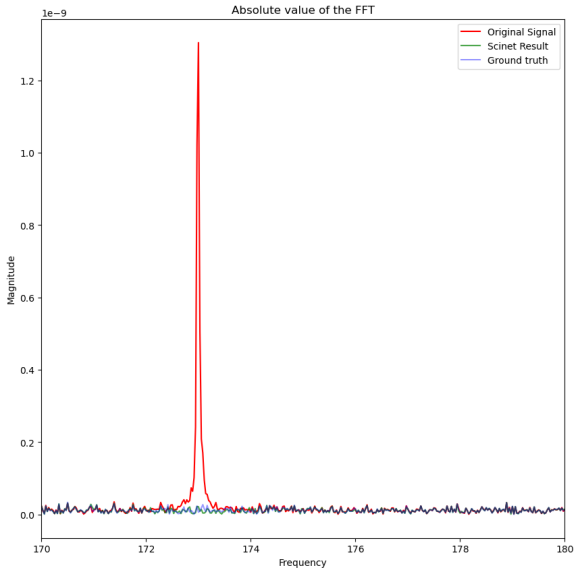

Figure 5.8: FFT Absolute value of the entry signal, the output, the ground truth

Another way of quantifying the effect of SCINet is to calculate the SNR by shifting the model signal by one time step to obtain the instant of detection. This method is used to estimate the various parameters of the bodies that generated the gravity wave.

The aim is to compare the SNR obtained before the addition of the violin peak with that obtained after the passage of SCINet. The closer the SCINet SNR is to the initial SNR, the less information about the gravitational wave will be removed.

The two SNR peaks are obtained at the 26th second, which already means that SCINet has not applied a time shift. The value of the original signal is 48.2 and that of the signal after SCINet is 47.9. This means that there is indeed a loss of signal in relation to the passage of SCINet.

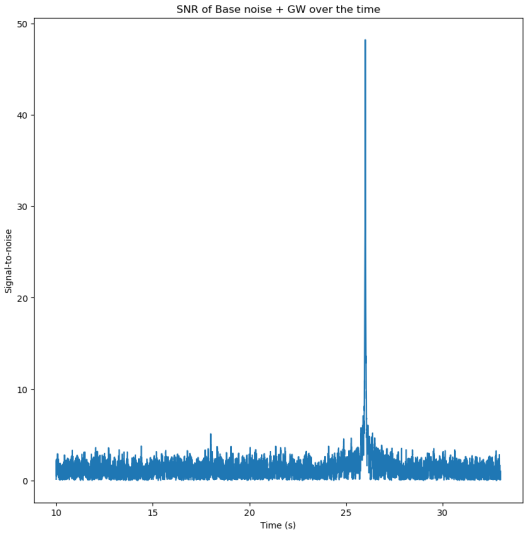

Figure 5.9: SNR over time of base noise and the gravitationnal wave

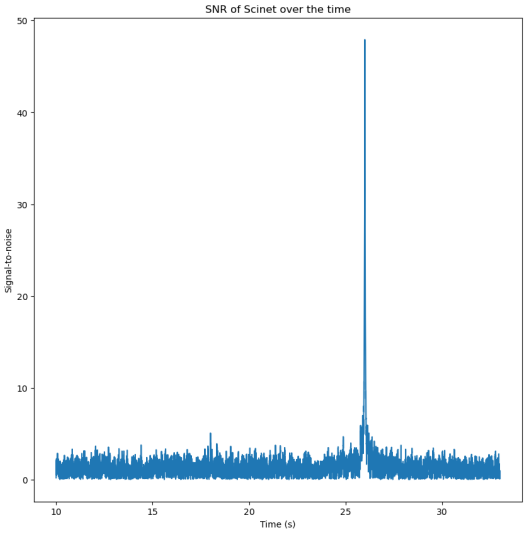

Figure 5.10: SNR over time of the SCINet output

6 Conclusion

This report presented a comprehensive survey of gravitational waves, from their theoretical foundations to the practical advances made possible by detectors such as LIGO, Virgo and KAGRA. After exploring the operation of gravitational interferometers and the challenges posed by suspension noise, particularly within the KAGRA experiment, the focus was on noise reduction techniques, in particular the suppression of thermal resonance peaks.

However, one of the key contributions of this work lies in the application of machine learning methods to the processing of detector data. Using SCINet, we have demonstrated the potential of deep learning to improve the detection and conditioning of gravitational data. The proposed model not only makes it possible to process efficiently the large quantities of data produced by interferometers, but also to better filter and analyze signals disturbed by suspension thermal noise.

The integration of machine learning in the field of gravitational waves represents a promising step forward. This work has highlighted the ability of these algorithms to identify subtle patterns in the data, be it one, two peaks or even a gravitational wave, paving the way for finer analysis and faster, more accurate detection of gravitational events. What's more, these tools can be used to generate synthetic datasets to simulate various scenarios and test new hypotheses, which is crucial for the ongoing improvement of detectors.

The results obtained show that the machine learning approach can make a significant contribution to improving the performance of current and future detectors. With prospects for continued technological evolution, it is likely that these methods will play a central role in the exploitation of gravitational data and the discovery of new astrophysical phenomena.

Future avenues of improvement would be to simulate real KAGRA noise, without the suspension thermal noise to be able to have a ground truth, and then add the violin noise to train a SCINet model on it. It would also have been interesting to apply different SCINet models to the 30 or so KAGRA peaks, to try and remove them in small groups and then reconstruct the signal.

In conclusion, this report highlights not only the advances made in gravitational wave physics, but also the growing importance of artificial intelligence techniques in this field. The work carried out paves the way for a wider integration of these approaches in future generations of detectors, promising even more significant discoveries in the years to come.

References

[1] B. P. Abbott et al. “Observation of Gravitational Waves from a Binary Black Hole Merger”. In: *Phys. Rev. Lett.* 116 (6 Feb. 2016), p. 061102. DOI: 10.1103/PhysRevLett.116.061102. URL: https://link.aps.org/doi/10.1103/PhysRevLett.116.061102.

[2] H Abe et al. “Performance of the KAGRA detector during the first joint observation with GEO600 (O3GK)”. In: *Progress of Theoretical and Experimental Physics* 2023.10 (June 2022). ISSN: 2050-3911. DOI: 10.1093/ptep/ptac093.

[3] S Chatterji et al. “Multiresolution techniques for the detection of gravitational-wave bursts”. In: *Classical and Quantum Gravity* 21.20 (Sept. 2004), S1809–S1818. ISSN: 1361-6382. DOI: 10.1088/0264-9381/21/20/024.

[4] A. Einstein and N. Rosen. “On gravitational waves”. In: *Journal of the Franklin Institute* 223.1 (1937), pp. 43–54. ISSN: 0016-0032. DOI: https://doi.org/10.1016/S0016-0032(37)90583-0.

[5] Lee Samuel Finn and Soma Mukherjee. “Data conditioning for gravitational wave detectors: A Kalman filter for regressing suspension violin modes”. In: *Physical Review D* 63.6 (2001), p. 062004. URL: https://arxiv.org/abs/gr-qc/0009012.

[6] Raban Iten et al. “Discovering Physical Concepts with Neural Networks”. In: *Physical Review Letters* 124.1 (Jan. 2020). ISSN: 1079-7114. DOI: 10.1103/physrevlett.124.010508.

[7] Guokun Lai et al. *Modeling Long- and Short-Term Temporal Patterns with Deep Neural Networks*. 2018. arXiv: 1703.07015 [cs.LG].

[8] Minhao Liu et al. *SCINet: Time Series Modeling and Forecasting with Sample Convolution and Interaction*. 2022. arXiv: 2106.09305 [cs.LG].

[9] Michele Maggiore. *Gravitational Waves. Vol. 1: Theory and Experiments*. Oxford University Press, 2007. ISBN: 978-0-19-171766-6, 978-0-19-852074-0. DOI: 10.1093/acprof:oso/9780198570745.001.0001.

[10] Michele Maggiore. *Gravitational Waves. Vol. 2: Astrophysics and Cosmology*. Oxford University Press, Mar. 2018. ISBN: 978-0-19-857089-9.

[11] Florent Robinet et al. “Omicron: A tool to characterize transient noise in gravitational-wave detectors”. In: *SoftwareX* 12 (July 2020), p. 100620. ISSN: 2352-7110. DOI: 10.1016/j.softx.2020.100620.

[12] Seiya Sasaoka. “Applications of convolutional neural network and Hilbert-Huang transform to gravitational-wave data analysis”. In: *Department of Physics, Tokyo Institute of Technology* (2024, FY2023). URL: https://www.gravity.phys.titech.ac.jp/thesis.html.